Online **ISSN :** 3049-3455

Mineral Metal Energy Oil Gas and Aggregate

Contents available at: *www.informaticsjournals.co.in/index.php/2MEOGA*

Scalable Graphene Oxide Composite for Cadmium Adsorption in Batch and Fixed-Bed Column Studies

Rishi Karan Singh Rathour[1,2*], Hemant Singh[1,3], Jayanta Bhattacharya[1,4,5*], and Abhijit Mukherjee[1,6]

[1]*School of Environmental Science and Engineering, Indian Institute of Technology Kharagpur, Kharagpur - 721302, West Bengal, India; jayantaism@gmail.com, rishi.nitd@gmail.com*
[2]*TCF-Lead Advisory, EY LLP Chandigarh UT, India*
[3]*Department of Civil Engineering, Galgotias University, Greater Noida - 203021, Uttar Pradesh, India*
[4]*Department of Mining Engineering, Indian Institute of Technology Kharagpur, Kharagpur - 721302, West Bengal, India*
[5]*Zelence Industries Pvt. Ltd., Kharagpur - 721302, West Bengal, India*
[6]*Department of Geology and Geophysics, Indian Institute of Technology Kharagpur, Kharagpur - 721302, West Bengal, India*

Abstract

Graphene-oxide (GO) based nanomaterials have been of tremendous interest for water pollutant removal in the past few decades. However, the high colloidal stability of GO limited its application potential to batch adsorption only because of its high pore-clogging nature and difficulty in post-treatment recovery when used as packing material in fixed-bed columns in continuous flow treatment. This work focuses on a facile approach for coating GO onto silica sand (SiS) by employing Polyvinyl-Alcohol (PVA) as adjoining material to form a stable SiS/PVA-GO composite. The spectroscopic and microscopic characterization revealed a randomly intercalated PVA-GO sheets matrix, uniformly wrapped onto the sand surface and forming interconnected pores. The batch adsorption of Cd^{2+} by SiS/PVA-GO followed the Pseudo-second-order kinetics and Freundlich isotherm. The maximum batch and fixed-bed-column adsorption capacities were 3.70 and 5.80 mg/g, respectively. Additionally, Cd^{2+} removal efficacy in the column at a varying initial concentration (Co), flow rate (Q), and bed height (h) demonstrated that the Number of Bed Volumes (NBV) treated decreased from 114 to 38 and 229 to 25, with increasing Q from 5-15 mL/min and Co from 10-30 mg/L, respectively. Further, non-linear fitting of breakthrough curves using the Thomas, Yoon–Nelson, Bed-Depth-Service-Time, and Dose-Response models revealed a good correlation. The BSDT model fitting raises the scope for upscaling. The post-adsorption composite characterization using XPS, EDS, and SEM, revealed the predominant adsorption forces were electrostatic, cation-π, and ionic interaction. Overall, this study demonstrates the SiS/PVA-GO as a promising material in the direction of GO-based adsorbent for wastewater treatment.

Keywords: *Breakthrough Curve, Cadmium Adsorption, Fixed-Bed Column, Graphene-Oxide-Sand Composite, Post-Adsorption Mechanism*

1.0 Introduction

Cadmium (Cd^{2+}) is a known toxic, mobile, and non-essential trace element found in the ecosystem. Cd^{2+} enters the environment through electroplating, smelting, metal refining, mining, and phosphate fertiliser industries, ranging from 15 - 1000 mg/L[1,2]. In the human body, Cd^{2+} mimics Ca^{2+}, and its chronic exposure is commonly associated with many health complications, e.g., cardiac arrest, breast and lung cancer, cerebral infection, and disorder in glucose metabolism[3,4]. Owing to the long biological life (15 to 30 years) and toxic nature, the World Health Organization has set the maximum allowable limit of Cd^{2+} to 3 µg/L in drinking water and monthly intake to 25 µg/kg body weight[5]. Currently, various treatment technologies are available for aqueous Cd^{2+} removal, e.g.,

membrane filtration, precipitation, adsorption, and ion exchange[6]. In the above available technologies, adsorption is commonly accepted due to its feasible treatment economics, easy operation, comparatively little sludge generation, no secondary pollutant generation, and most importantly, reusability[7,8]. In adsorption processes, the batch mode of operation is widely practised to determine the adsorption potential of the adsorbents[9-12]. However, due to the small volume treatment capacity and high monitoring requirement, the batch process is rarely applied in industrial wastewater treatment[13]. In contrast, the fixed-bed column mode of adsorption is widely applied to treat large volumes of wastewater because of its low monitoring requirements and continuous process[13-15]. Several adsorbent materials, like activated carbon, processed agriculture biomass, biochar, iron oxides, etc., have been tested in batches and columns for Cd^{2+} and other water pollutants[7]. However, these adsorbents fail in scale-up challenges due to high production costs, slow sorption kinetics, environmental transformation, and poor regeneration[13,14,16]. Hence, developing a novel, effective, and exceedingly solvent-stable adsorbent with excellent regeneration capability is imperative to meet the application requirements.

The recent developments have delivered several novel nanomaterials with exceptional properties with extremely high surface-to-volume ratio, numerous functional groups, rapid adsorption kinetics, and superior sorption capacity with regenerative potential[17-19]. Due to their prospective applications in water and wastewater remediation, Graphene Oxide (GO) and its composites have attracted enormous scientific interest[20-22]. To address the existing challenges of graphene application, current research has also been reported on developing GO-based three-dimensional (3D) aerogels[23,24]. However, the inherent fragility of GO-based aerogels in aqueous media is prone to collapse, limits their cyclic use, and causes secondary pollution of the water environment[25].

Supporting GO on a substance with a higher granulometry is a compelling option, and Sand is cost-effective and beneficial due to its higher granulometry, non-toxic, environmentally benign nature[25,26]. Sand has already been proven to be an excellent supporting medium for GO in various literature, where Gao *et al.*[27] and Gong *et al.*[28] coated GO onto the sand surface through thermal annealing and found better adsorption efficiency toward heavy metals and dyes. The coating of GO on the Sand through physical mixing followed by moderate heating has resulted in weak bond formation at the interface; consequently, GO layers washed out easily from Sand in an aqueous medium under moderate agitation or high-pressure conditions. Similarly, the chemical routes of GO-sand complex preparation are chemical, labour, and energy-intensive processes[27-29]. Hence, developing an alternative route or modifying the existing method is imperative to make the process scalable and sustainable.

Here, an attempt has been made to develop a ternary composite of GO-coated Silica sand (SiS) via PVA crosslinking (SiS/PVA-GO). PVA is a flexible, non-toxic, water-soluble, and cheap polymer with a remarkable ability to form inter and intra-molecular hydrogen bonding[30,31]. Thus, PVA was selected to strengthen the composite stability in an aqueous medium and reduce the overall cost of the adsorbent. The as-proposed route for composite preparation does not demand any additional chemical or heat treatment, indicating its scalability and eco-friendly nature. The influence of pH, initial Cd^{2+} concentration, and SiS/PVA-GO dose was investigated under batch tests. In contrast, the effect of variations of flow rate, bed height, and initial concentrations was explored in continuous fixed-bed column studies. Besides, the experimental outputs for batch and column studies were evaluated using well-established batch and column kinetics and isotherm models. Additionally, the mechanism of Cd^{2+} adsorption by SiS/PVA-GO was determined via its post-adsorption characterization.

2.0 Materials and Methods

2.1. Materials

Graphite powder of particle sizes ≤ 50 µm and PVA were acquired from Loba Chemie., India. Sulfuric acid (H_2SO_4, 98%), Phosphoric acid (H_3PO_4, 85%) Potassium permanganate ($KMnO_4$), Hydrogen peroxide (H_2O_2, 30%), Hydrochloric acid (HCl, 36%), and cadmium sulfate ($3CdSO_4{\cdot}8H_2O$) were obtained from Merck India. Silica Sand (SiO_2) of 50-70 mesh size was procured from Sigma-Aldrich. Deionized (DI) water, with conductivity ≥ 18 MΩ/cm was used throughout the experimental study.

2.2. Synthesis of SiS/PVA-GO

The improved Hummers method was used to synthesize GO, as previously reported[22,32] The solution of PVA-GO

was made by vigorously mixing the individual PVA (10 mg/mL) and GO (10 mg/mL) solutions together and subsequently bath sonicating (phoenix ultrasonic bath, frequency 50 kHz, power 35 W, voltage 220 V) them for 30 minutes. The coating of PVA-GO onto the sand surface[22] was accomplished by pouring the PVA-GO solution (10 mL) on a glass petri dish containing 1.5 g of sand particles, followed by transferring the petri dish to a vacuum oven for 12 h at 60°C. The petri dish containing the final product as SiS/PVA-GO was withdrawn from the oven, collected by scraping the material through a spatula, and kept in a glass bottle. The as-prepared SiS/PVA-GO was used without any modification for Cd^{2+} adsorption from an aqueous solution. The schematic presentation for the SiS/PVA-GO preparation method is shown in Scheme 1.

2.3. Instrumental Characterization

Details of the various instruments used for the characterization of SiS/PVA-GO pre and post-adsorption have been provided in the Supporting Information (S2).

2.4. Batch Adsorption Study and Theory

Details of the batch adsorption study, theories of adsorption kinetics and isotherm, and other calculations, e.g., Cd^{2+} removal (%) and the SiS/PVA-GO adsorption capacity, are explained in the Supporting Information (S3).

2.5. Data Interpretation for Fixed-Bed Column Adsorption

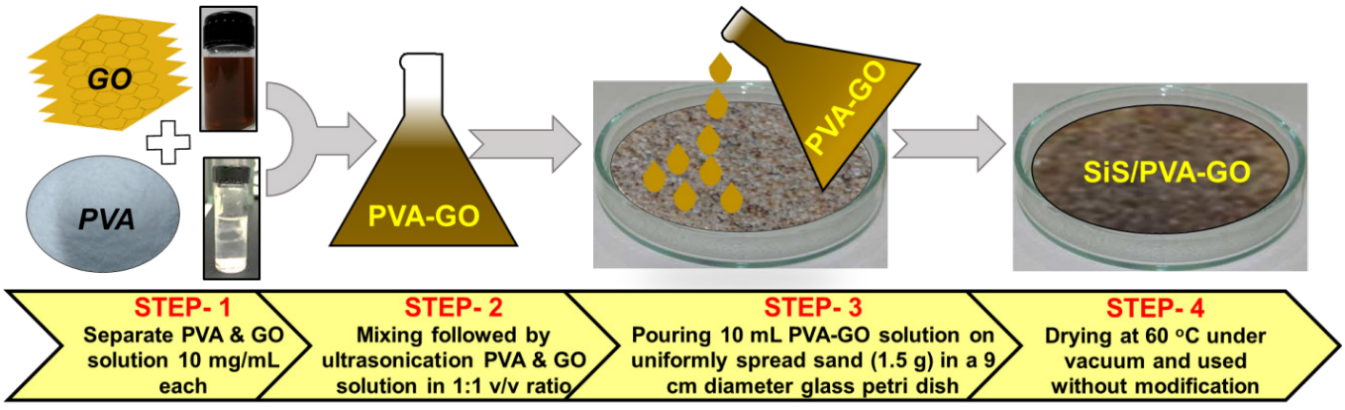
The fixed-bed column adsorption experiments were conducted in a 1.0 cm diameter glass column with a height of 20.0 cm (column setup in Figure 1). The parameters, i.e., flow rates (5, 10, and 15 mL/min), bed heights (5, 10, and 15 cm), and initial Cd^{2+} concentrations (10, 20, and 30 mg/L), were used in column investigation. The weight of SiS/PVA-GO for each 5, 10, and 15 cm of bed height was found to be 5.0, 10.5, and 15.0 g, respectively. To prevent adsorbent loss during the continuous flow, the column was plugged with glass wool on top and bottom of the adsorbent. The peristaltic pump (Model no. pp-30-2C–EX of Miclins, India) maintains the upward flow in the column. The duration of contact between adsorbent and adsorbate (Empty Bed Contact Time (EBCT)) was computed using Equation (Eqs.) 1 and found to be 0.78, 0.39, and 0.26 minutes, respectively, for 5, 10, and 15 mL/min. During the fixed-bed column study, the pH and temperature were fixed to 8.8 ± 0.3 and 25.0 ± 3°C. The Cd^{2+} removal efficiency in the column was considered by monitoring the Breakthrough Curves (BTC). A BTC is expressed as a plot of the normalized concentration (C_t/C_o) vs. time. The time 't' when Cd^{2+} attained 0.04 mg/L effluent concentration was referred to as the breakthrough time (t_B), whereas the exhaust time (t_E) was considered for concentration >99 per cent or $C_o \geq 19.0$ mg/L.

$$EBCT = \frac{Z \times S}{Q} \quad (1)$$

The volume of liquid (V_{eff}) (Eqs. 2) and mass of solute (m_{total}) (Eqs. 3) were calculated with the equations:

$$V_{eff} = Q \times t_{total} \quad (2)$$

$$m_{total} = \frac{C_o \times Q \times t_{total}}{1000} \quad (3)$$



Scheme 1. Prepration of SiS/PVA-GO.

The Cd^{2+} adsorbed amount (q_{total}) onto the SiS/PVA-GO bed and maximum adsorption capacity (q_{eq}) were determined via Eqs. 4 and 5, respectively.

$$q_{total} = \frac{Q}{1000W}\int_{0}^{t_{total}} (C_0 - C_t)dt \quad (4)$$

$$q_{eq} = \frac{q_{total}}{W} \quad (5)$$

The Mass Transfer Zone (MTZ) and the Number of Bed Volumes treated (NBV) were measured from Eqs. 6 and 7, respectively.

$$H_{MTZ} = Z\left[1 - \frac{t_B}{t_E}\right] \quad (6)$$

$$\text{NBV} = \frac{\text{Volume of water pass through breakthrough point}}{\text{Volume of adsorbent bed}} \quad (7)$$

The percentage removal (%R) of Cd^{2+} is calculated using Eqs. 8.

$$\%R = \left(\frac{q_{total}}{m_{total}}\right) \times 100 \quad (8)$$

The notations used in Eqs. 1 to 8 are as follows: Q (mL/min) = volumetric flow rate; C_o (mg/L) and C_t (mg/L) are the Cd^{2+} concentrations at t = 0 and t = t, respectively; $t_{(total)}$ = total flow time (min); W (g) = weight of the SiS/PVA-GO; Z (cm) = column fixed-bed height; S (cm^2) = column cross-sectional area.

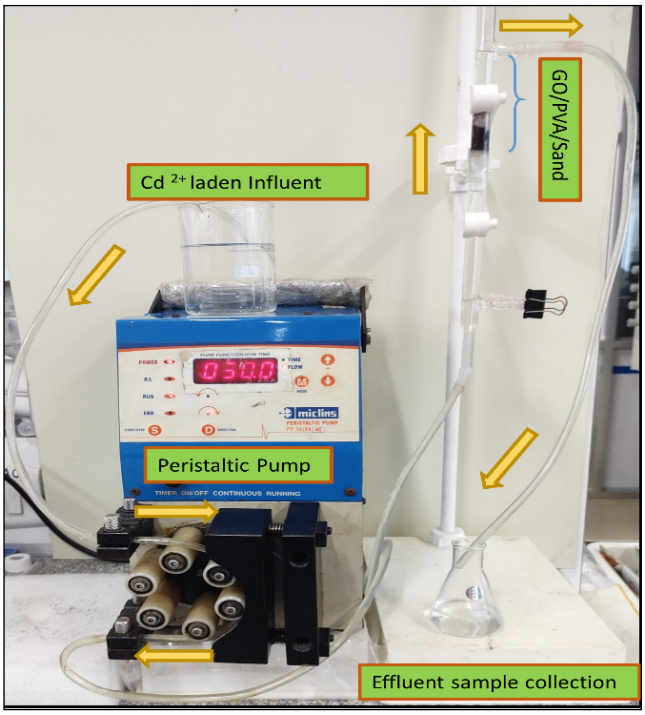


Figure 1. Fixed-bed column setup for the adsorption of Cd^{2+} by SiS/PVA-GO.

3.0 Results and Discussion

3.1. Characterization of SiS/PVA-GO

The morphology study of GO using FESEM (Figure 2a) revealed smooth surfaces, interlayer voids, and single-layer sheets, indicating successful exfoliation of graphite into GO[33]. The micrograph of pure sand particles is provided in Supplementary Figure S1 to understand the coating of the GO-PVA. Furthermore, the folded GO sheets were detected on the surface of SiS/PVA-GO (Figure 2b), indicating the creation of an interconnected network via a hydrogen bond between the -OH groups of PVA and GO surrounding the sand particles[34,35]. Furthermore, the dispersal of GO on the PVA matrix was investigated via tapping mode AFM. Figures 2c and 2d show 2D and 3D topography images of PVA-GO, respectively. The PVA-GO developed a rough and irregular surface (Figure 2c), confirming the SEM result of uniformly dispersed but randomly ordered GO-sheets in the PVA matrix. Furthermore, a "ridge-and-valley" morphology (Figure 2d) depicts a widely connected network of PVA-GO that could facilitate water diffusion and active site accessibility of the SiS/PVA-GO[35,36].

Meanwhile, the XRD scans of the precursors GO, PVA, PVA-GO, and SiS/PVA-GO are shown in Figure 2e. The individual peak at 2θ = 12.53° associated with d-spacing = 0.71 nm describes the peak from the (002) plane of GO[37,38]. While the typical peak at 2θ = 19.75° and shoulder ~ 22.6° corresponding to d=0.45 and 0.36 nm represent PVA[39]. However, following GO incorporation into the PVA matrix, the PVA-GO exhibited a contracted peak at ~19.2°, demonstrating the changes in crystallinity of the materials[40,41]. Additionally, the PVA-GO spectra's lack of any additional peaks indicates that GO sheets are evenly distributed throughout the PVA matrix[42]. Besides, the peaks at 21.07 and 26.88 in the SiS/PVA-GO could be allocated to the characteristic peaks of SiO_2[43,44], while the absence of the distinctive peaks of GO and PVA in the SiS/PVA-GO might be due to their low mass loading as compared to the Sand.

The functional groups on the GO, PVA, PVA-GO, and SiS/PVA-GO surfaces were identified via FTIR scans (Figure 2f). The distinctive peaks at 3414, 1723, 1631, 1385, and 1122 cm^{-1} attributed to the stretching of the O–H bond of the hydroxyl group, C=O bond of the carboxyl group stretching, bending of aromatic C=C, stretching of phenolic C-O, and epoxy C-O-C stretching of GO, respectively[32,33]. The individual PVA peaks occurring at 3448 and 1108 cm^{-1} allocated to C-O and –OH vibration, respectively[31]. Further, the PVA-GO

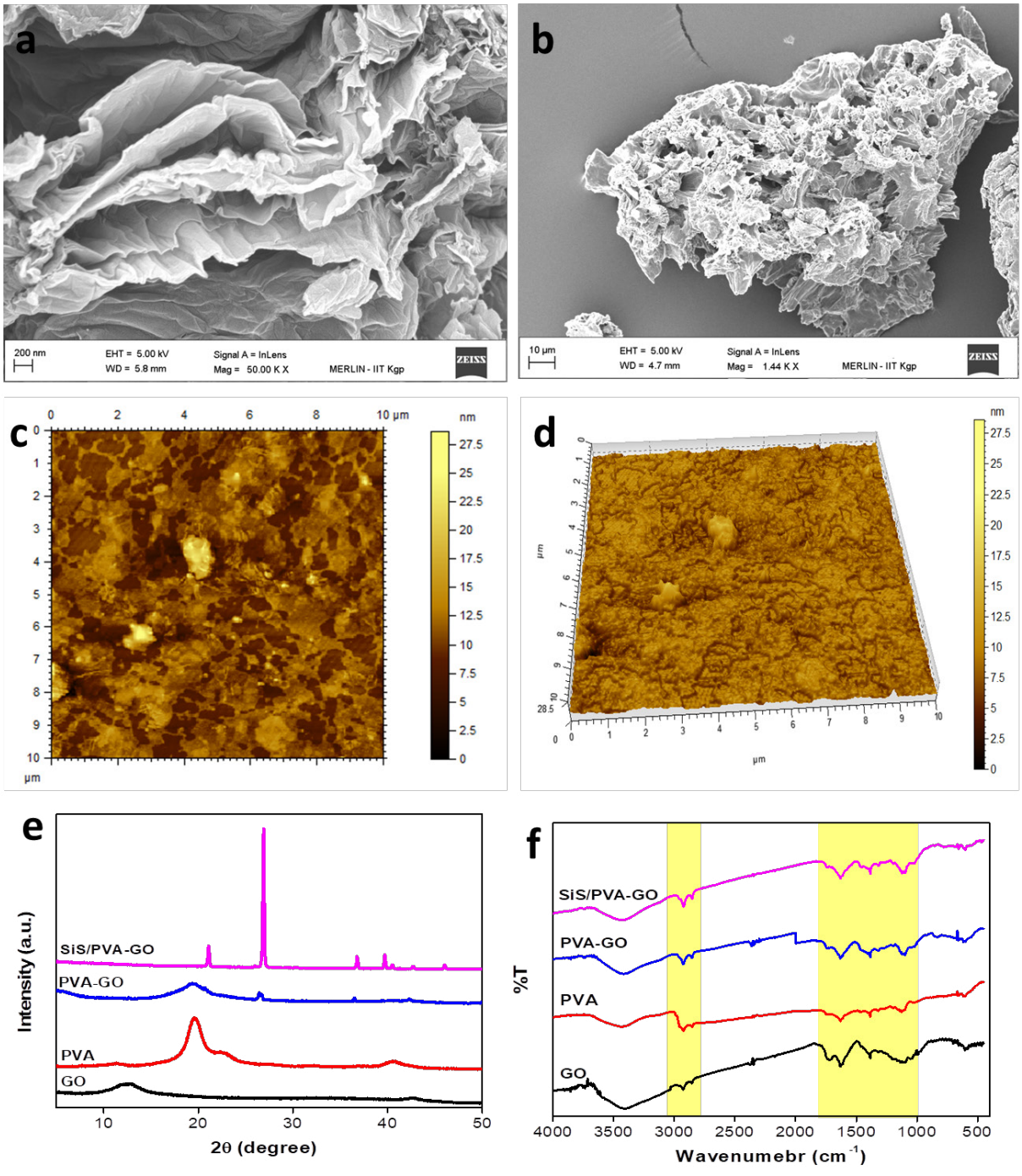


Figure 2. Surface morphology imaged from FESEM (a) GO and (b) SiS/PVA-GO; AFM image of PVA-GO (c) 2D profile and (d) 3D profile; (e) XRD spectra, and (f) FTIR spectra.

spectra show no apparent change in the peak position; however, the corresponding peaks were weakened due to inter/intramolecular hydrogen bonding between PVA and GO molecules, indicating that the functional groups of both the molecules were preserved. Similarly, in the SiS/PVA-GO, the peaks ~3400, 1723, and 1630 cm^{-1} were weak, which could be due to inter/intramolecular hydrogen bonding. Also, the peak at 1019 cm^{-1} of SiS/PVA-GO is credited to the stretching vibration of Si-O-Si[44,45]. The BET surface area, pore volume, and pore size of SiS/PVA-GO were measured to be 0.16 m^2/g, 0.0003 cm^3/g, and 6.76Å, respectively. The low surface area could be attributable to the low bulk deposition of the PVA-GO onto the sand surface (weight ratio of GO-PVA to Sand = 1:15). The adsorbent surface area plays a significant role in pollutant adsorption, but other characteristics, such as quantum of functional groups on the adsorbent, electronic density, affinity between the adsorbate and adsorbent are also crucial in pollutant removal[46].

3.2. Batch Adsorption Experiments

3.2.1. Effect of Solution Ph and Adsorbent Dose

The solution pH is a vital factor in adsorption studies, as it influences the ionization of metal ions and adsorbents[47]. Hence, the effect of pH (2±0.3 – 8.8±0.3) on Cd^{2+} adsorption by SiS/PVA-GO was assessed and shown in Figure 3a. The zeta potential of GO was found to be ≥ -30 between pH 2 to 12, in our prior study[33]. Further, the zeta potential of SiS/PVA-GO has a negative charge throughout the entire pH range (as given in Figure S2). The %R increased from 3.0-81.8% and the corresponding q_e from 0.3 to 3.0 mg/g with a rise in pH from 2±0.3 to 8.8±0.3, respectively. The increase in %R or q_e with an increase in pH could be due to electrostatic attraction between the oppositely charged adsorbent surface and adsorbate molecules[48]. The lesser adsorption efficiency at lower pH could be due to competition between Cd^{2+} and H_3O^+ ions for finite no of adsorption sites onto SiS/PVA-GO[47,49]. The variation in SiS/PVA-GO dose (1.0 to 11.0 g/L) has also resulted in a significant change in its %R and q_e as shown in Figure 3b. As the dose of SiS/PVA-GO increases from 1.0 to 5.0 g/L the %R of Cd^{2+} rises from 8.9% (q_e=1.8 mg/g) to 73.0% (q_e = 2.9 mg/g), respectively, which could attribute to the presence of high surface area and a large number of active sites[50]. However, further increasing the adsorbent dose (7.0 - 11.0 g/L) had no significant effect on %R (75.4 to 84.6) and q_e (2.1 and 1.53 mg/g). The reason for this behaviour could be attributed to the presence of more unoccupied sites after adsorption equilibrium has been achieved. Similar results were also reported previously by Kango and Kumar 2016, Medina *et al.* 2016; we determine the effects of different concentrations of GO in the nanocomposite, as well as the role of pH and nanocomposite load in Pb^{2+} removal. The mechanisms of sorption and diffusion of lead in this new nanocomposite, as well as its reusability after regeneration were also investigated. The results show that the addition of GO into the polymer blend has increased significantly the metal uptake capacity owing to the additional oxygen-containing functional groups present in GO and the increase in surface area. Additionally, the solution pH affected the nanocomposite adsorption, with the best adsorption occurring at pH 5. The most economical adsorbent loading was determined to be 37.5 g of hydrogel beads per liter of solution. The pseudo second-order model best described the adsorption kinetics and determined that chemisorption was the mechanism of lead removal. The diffusion mechanism of this new nanocomposite was determined using the intraparticle diffusion model, which suggested that adsorption occurred in three distinct phases. The adsorption isotherms for the hydrogel beads all showed excellent fit to the Langmuir isotherm model. The CS–PAA beads with 5% GO presented the highest Pb^{2+} adsorption capacity (138.89 mg g^{-1}, Fan *et al.* 2008 and Salih *et al.* 2019 kinetics and thermodynamics of Cd(II)[51-54]. Hence, the adsorbent dose of 5.0 g/L was fixed for subsequent batch adsorption experiments.

3.2.2. Adsorption Kinetics and Isotherm

The adsorption kinetics of Cd^{2+} onto SiS/PVA-GO was conducted at different concentrations (10, 20, and 50 mg/L), and the calculated parameters are shown in Table 1. It was noticed that the Cd^{2+} sorption rate was very rapid in the initial 20 min and reached the plateau within 30 min (Figure 4a). Further, any additional extension of contact time resulted in no improvement in the qe or %R of Cd^{2+}. Yet, another contact time (180 min) was chosen for further studies to guarantee complete equilibrium. This rapid adsorption in the initial stage could be due to the accessibility of many sorption sites, which progressively occupied and resulted in a slower sorption rate[46]. Also, the quick adsorption is ascribed to interconnected

pores formed by an arbitrary arrangement of GO in the PVA matrix[2,33]. The non-linear regression analysis of experimental data using Pseudo-First-Order (PFO) (Eqs. S4), Pseudo-Second-Order (PSO) (Eqs. S5), and Elovich (Eqs. S6) kinetic models are displayed in Table 1. The PSO showed an excellent correlation between the experimental and model-predicted adsorption capacity and high R^2 and low χ^2 values. Therefore, showing the PSO better explains the adsorption kinetics, and so, the adsorption of Cd^{2+} onto SiS/PVA-GO occurred through electron exchange. The PSO rate constant (k_2) at 10, 20, and 50 mg/L was calculated to be 0.763, 0.666, and 0.254 g/mg×min, respectively, indicating that Cd^{2+} adsorption rate constant decreases with a rise in initial Cd^{2+} concentration of from 10 to 50 mg/L. The fall in k_2 with an increase in Cd^{2+} concentration could be explained by the behaviour of a limited number of active sites present in the adsorbent. The active sites carrying high energy are occupied faster, and the remaining active sites having low energy are occupied later, hence the rate constant falls with an increase in initial concentration as the ratio of the available number of active sites to the available number of Cd^{2+} ions falls[55]. The mass transfer process was described using Weber-Morris Intraparticle Diffusion (ID) model (Eqs. S6)[38,56]. The ID plot (Figure 4b) revealed that adsorption occurs in two steps; the 1st one is the migration of Cd^{2+} from solution to the surface of the SiS/PVA-GO, while 2nd is the diffusion of Cd^{2+} through pores to the adsorption sites. Cd^{2+} in solution.

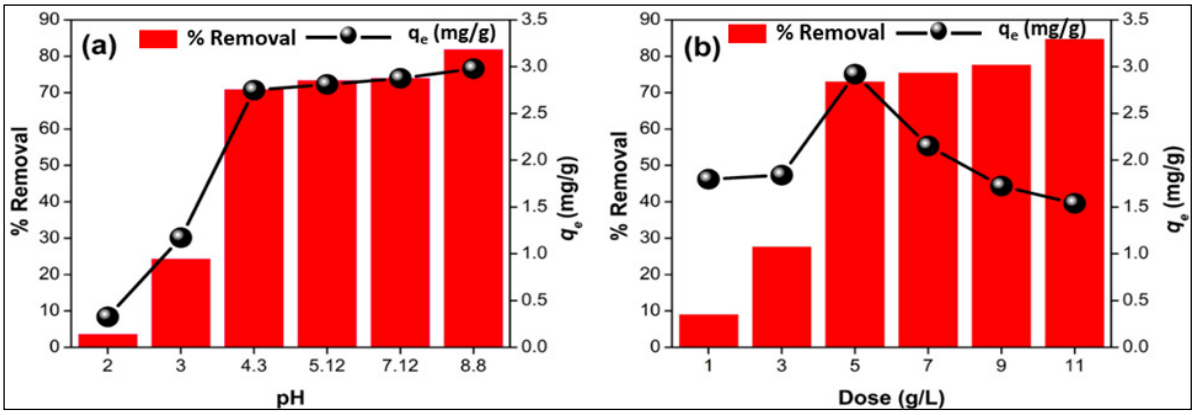


Figure 3. Effect of individual parameters on the adsorption (a) pH and (b) Dose study of SiS/PVA-GO. Conditions: Cd^{2+} C_o = 20 mg/L, Temp = 30 °C, and SiS/PVA-GO dose = 5.0 g/L, at optimized pH = 8.8 ± 0.3).

Table 1. Kinetic constants of Cd^{2+} adsorption by SiS/PVA/GO

PFO						PSO				
C_o (mg/L)	$q_{e,Exp}$ (mg/g)	k_1 (1/min)	$q_{e,cal.}$ (mg/g)	χ^2	R^2	k_2 (g/mg*min)	$q_{e,cal.}$ (mg/g)	χ^2	R^2	
10	1.62	0.491	1.49	0.011	0.957	0.763	1.54	0.007	0.972	
20	2.04	0.435	1.95	0.006	0.985	0.666	1.99	0.004	0.989	
50	3.82	0.397	3.59	0.041	0.972	0.254	3.70	0.019	0.987	
Elovich model						**Intraparticle diffusion model**				
C_o (mg/L)	α (mg/g/min)	β (g/mg)	χ^2	R^2	k_{ip1} (mg/g×min$^{0.5}$)	k_{ip2} (mg/g×min$^{0.5}$)	C_{i1}	C_{i2}	R_1^2	R_2^2
10	5.7×10^5	13.19	0.003	0.967	0.020	0.029	1.315	1.252	0.556	0.786
20	5.6×10^8	13.72	0.004	0.971	0.062	0.036	1.626	1.604	0.957	0.841
50	1.1×10^6	5.45	0.011	0.972	0.146	0.041	2.788	3.265	0.870	0.885

Where, C_o = Initial Concentration, $q_{e,Exp}$ = Experimental adsorption capacity, k_1, k_2, and k_{ip} are the respective rate constants. C = constant. α = initial sorption rate, β = constant related to chemisorption in the Elovich model.

Table 2. Cd^{2+} adsorption on SiS/PVA-GO isotherm study parameters

Langmuir						Freundlich				Temkin			
Temp. (°C)	$q_{m, Exp.}$ (mg/g)	$q_{m\ cal.}$ (mg/g)	K_L (L/mg)	χ^2	R^2	K_F ((mg/g)/(l/mg)$^{1/n}$)	1/n	χ^2	R^2	b_T (kJ/mol)	A_T (L/mg)	χ^2	R^2
30	1.84	1.82	1.51	0.007	0.528	1.35	10.30	0.005	0.699	1.6×10^4	4.7×10^3	0.004	0.677
40	2.79	3.05	0.35	0.024	0.889	1.17	3.36	0.020	0.978	4.3×10^3	4.768	0.011	0.946
50	3.69	3.90	0.45	0.138	0.788	1.50	3.11	0.098	0.927	3.5×10^3	6.157	0.083	0.878

Where, q_m = maximum adsorption capacity. K_L K_F, and b_T are the respective isotherm constants. A_T = equilibrium binding constant. n = heterogeneity factor (Freundlich isotherm).

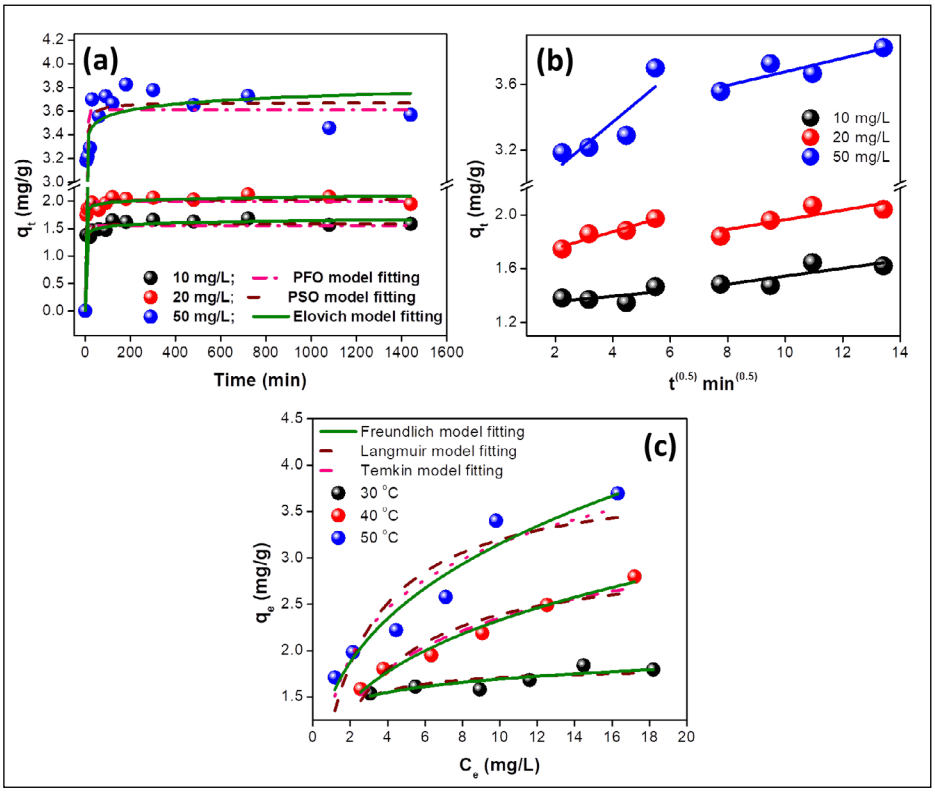


Figure 4. (a) Non-linear kinetic model fitting and (b) IPD; (Conditions: Dose = 5 g/L, Stirring = 170 rpm, pH = 8.8±0.3, and Temp = 30°C), (c) Non-linear isotherm fitting (Conditions: At stirring = 170 rpm and pH = 8.8±.3, initial Cd^{2+} concentration = 20 mg/L at doses = 1-11 g/L).

Table 3. Comparative study of SiS/PVA-GO with similar adsorbents for Cd^{2+} removal

Adsorbent	Cd(II) Conc.	Equilibrium time (min)	q_m (mg/g)	Ref.
$MBC800\text{-}0.6_{300}$	10–150 mg/L	360	46.90	[49]
Mussel Shells	29.4 mg/L	120	26.0	[57]
Halomonas BVR1 immobilized in rGO	50-500 mg/L	180	20.30	[58]
Graphene-polymer adsorbent, GPHM	20 mg/L	2-30	10.67	[50]
Dry cyanobacterium Aphanothece sp cultivar	1-4.85 mg/L	N/A	8.20	[59]
Crab shell	0.58-12.16 mmol/L	1440	3.34	[60]
SiS/PVA-GO	10-30 mg/L	30	3.69	This study

To understand Cd^{2+} adsorption behaviour on SiS/PVA-GO, the adsorption isotherm at 30, 40, and 50°C was performed. The isotherm models, namely Langmuir (Eqs. S8), Freundlich (Eqs. S9), and Temkin (Eqs. S10), were applied to the experimental data[37,56]. Table 2 displays the parameters from the non-linear regression analysis and the respective plot is shown in Figure 4c. The best-fitted model was selected by comparison of R^2 and χ^2 values. The high R^2 (0.699 to 0.978) and low χ^2 (0.05 to 0.09) of the Freundlich model displayed the best fit to the experimental data. Hence, suggests that Cd^{2+} adsorption happened in multilayer form on heterogeneous SiS/PVA-GO surfaces. Further, with the increase in temperature from 30 to 50°C, the k_F ((mg/g)/(l/mg)$^{1/n}$) increased from 1.35 to 1.50, confirming that adsorption w favoured at the temperature[37,56]. The sorption potential of the SiS/PVA-GO improved from 1.84 to 3.69 mg/g by enhancing temperature from 30 to 50°C, corresponding to the endothermic nature of the adsorption. Furthermore, a comparison is presented for the Cd^{2+} adsorption capacity of SiS/PVA-GO with other similar adsorbents in Table 3. Although the adsorption capacity of the SiS/PVA-GO is lower than some of the similar adsorbents, the other adsorbents have limitations with continuous flow treatment and upscaling issues. SiS/PVA-GO can be applied for continuous flow adsorption-based treatment while having the potential for further upscaling and industrial application.

3.3. Fixed-Bed Column Adsorption

The continuous wastewater treatment systems on an industrial or laboratory scale rely heavily on operational parameters, including flow rates (Q), bed height (Z), and inlet concentration (Co). Therefore, to evaluate the efficiency of the SiS/PVA-GO, the breakthrough curve of Cd^{2+} under different working conditions was examined. As pH = 8.8±0.3 was selected during the batch study, hence, the same pH was kept constant throughout column experiments.

3.3.1. Effect of Bed-Height

The breakthrough curves of Cd^{2+} adsorption in the column were assessed at 5 to 15 cm bed heights, 10 mL/min flow rate, and 20 mg/L inlet Cd^{2+} concentration. It can be deduced from Figure 5a that the breakthrough (t_B) and exhaust (t_E) time improved from 20 to 150 min and 270 to 630 min, correspondingly, with a rise in bed height from 5 to 15 cm (Table 4). The outcome indicates the presence of additional adsorption sites because a greater amount of adsorbent was utilized for larger bed heights[61]. Also, a higher bed-height solution gets more retention time and minimizes the axial dispersion effect; hence, larger t_B and t_E were achieved[61,62]. In contrast, at smaller bed heights, axial dispersion governs the mass transfer, which results in Cd^{2+} inadequately diffusing through the column and causing a fall in the t_B and t_E. The MTZ, NBV, and q_{eq} increased from 4.6 to 11.4 cm, 50 to 127, and 5.19 to 5.80 mg/g, with an increase in bed-height from 5 to 15 cm, respectively, corresponding to an increase in the number of sorption sites and solute retention time with a surge in bed-height. But, as in this study, the increase in q_{eq} was very nominal even after increasing bed height 3-fold, which indicates that the mass transfer resistance also increases with a rise in bed height. Nonetheless, the flow rate of 10 mL/min partially overcomes the mass transfer resistance; hence, q_{eq} increased moderately[57,59].

3.3.2. Effect of Flow Rate

The Breakthrough Curve (BTC) of Cd^{2+} adsorption at 5, 10, and 15 mL/min flow rate is shown in Figure 5b, and the calculated parameters are shown in Table 4. It was observed that by increasing the flow rate, t_B and t_E declined from 90 to 10 min and 420 to 210 min, respectively. This indicates that the adsorption occurs in two stages: during the 1st stage- Cd^{2+} migrates from the bulk solution to the surface of SiS/PVA-GO, while through the 2nd stage, the diffusion of Cd^{2+} occurs at the sorption sites[59,63]. Furthermore, it was discovered that at a lower flow rate, the BTC becomes very smooth, and the column exhausts slowly due to a smaller amount of adsorbate flowing into the column, as a result, progressively saturating the adsorbent in the column. In contrast, the curve becomes steeper at a higher flow rate, and the column exhausts rapidly. It was also seen that increasing the flow rate three-fold, the NBV treated falls by three times from 114 to 38, and q_{eq} declines from 5.21 to 4.99 mg/g, attributed to inadequate contact time between Cd^{2+} and SiS/PVA-GO[57,61].

3.3.3. Effect of Cd^{2+} Concentration

Three concentrations of Cd^{2+} 10, 20, and 30 mg/L with optimized flow rate (10 mL/min) and bed height (5 cm) were studied. The breakthrough curve at

different concentrations is shown in Figure 5c, and the corresponding column parameters are presented in Table 4. The breakthrough displays that with an increase in initial Cd^{2+} concentration from 10 to 30 mg/L, the $t_{B,}$ and t_E, decreased from 90 to 10 min and 360 to 240 min, respectively. Similarly, the NBV treated also decreased nine-fold from 229 to 25 with an increase in initial concentration from 10 to 30 mg/L, respectively. This drop in NBV, $t_{B,}$ and t_E, signifies that higher Cd^{2+} concentrations rapidly saturate the column by quickly occupying the active sites of the SiS/PVA-GO due to a high mass transfer gradient[57]. Subsequently, q_{eq} increased from 4.02 to 5.63 mg/g as the initial concentration of Cd^{2+} increased from 10 to 30 mg/L, indicating that a higher influent concentration enhanced the mass loading of adsorbate into the column, resulting in a greater mass

Table 4. Fixed-bed column design parameters for Cd^{2+} adsorption

Q (mL/min)	Z (cm)	C_o (mg/L)	t_B (min)	t_E (min)	EBCT (min)	MTZ (cm)	NBV	m_{total} (mg)	V_{eff} (mL)	q_{total} (mg)	q_{eq} (mg/g)	%R
5	5	20	90	420	0.79	3.92	114	42.00	2100	26.07	5.21	62.1
10	5	20	20	270	0.39	4.63	50	54.00	2700	25.81	5.19	47.8
15	5	20	10	210	0.26	4.72	38	63.00	3150	24.97	4.99	39.63
10	10	20	30	450	0.79	9.33	38	90.00	4500	55.70	5.31	61.89
10	15	20	150	630	1.18	11.43	127	126.0	6300	87.04	5.80	69.08
10	5	10	90	360	0.39	3.75	229	36.00	3600	20.13	4.02	55.92
10	5	30	10	240	0.39	4.79	25	72.00	2400	28.17	5.63	39.18

Q = Flow rate, Z = Bed height, Co = Initial concentration, t_b = breakthrough time, t_e = equilibrium time, EBCT = empty bed contact time, %R = Percentage removal, MTZ = Mass transfer zone, V_{eff} = treated volume.

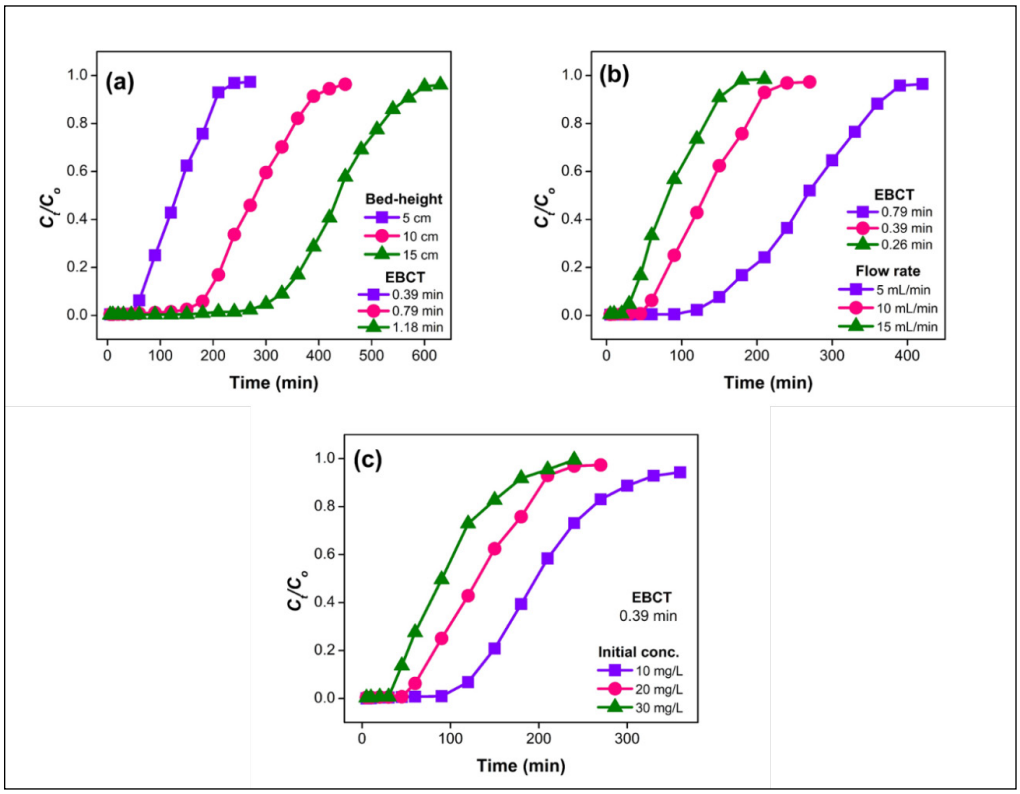


Figure 5. The Breakthrough curve of Cd^{2+} adsorption for (a) bed height, (b) flow rate, and (c) feed concentrations (conditions: pH = 5.5; Temperature = 25±3 °C).

driving force. However, it would be unwise to increase or decrease the initial concentration to increase the sorption capacity of adsorbents because higher adsorbate concentration reduces the exhaust time and regeneration potential. Similarly, the MTZ, mass transfer resistance, and adsorbent exhaust rate are also reduced at lower initial concentrations. Thus, an appropriate or intermediated concentration range is crucial for a certain bed height and flow rate[61,64].

3.4. Breakthrough Curve Modeling

To further understand the dynamic behaviour of Cd^{2+} adsorption and discover significant parameters for scale-up, it is imperative to predict the breakthrough curve. Therefore, the Thomas, Yoon-Nelson, Bed Depth Service Time (BDST), and Dose-Response (D_R) models[15,59,61] were used to assess the experimental data obtained at different initial concentrations, flow rate, and bed height.

3.4.1. Thomas Model

Thomas's model is incredibly helpful in characterizing the concentration profile of fixed-bed adsorption. This model was established from the conservation of mass in the flow system and is based on two fundamental assumptions- (1) adsorption equilibrium follows the Langmuir isotherm model and does not consider axial dispersion, and (2) the rate of sorption process follows PSO kinetics. Thomas's model is effective in examining the sorption capacity of an adsorbent at higher concentration ranges and may not give precise predictions at lower adsorbate concentrations[59,61]. The Thomas model's mathematical formulation can be found in Eqs. 10.

$$\frac{C_t}{C_o}=\frac{1}{1+\exp\left(\frac{k_{TH}*q_o*W}{Q}\right)-(k_{TH}*C_o*t)} \quad (10)$$

where k_{Th} (L/mg×min) and q_o (mg/g) are denoted as rate constant and sorption capacity, respectively. Whereas W (g) is the adsorbent weight Q (mL/min) is the flow rate, and t (min) is the run time of the column, respectively.

Figure 6.1 (a-c) presents a non-linear regression plot of the Thomas model, and parameters calculated from the plot of Cd^{2+} adsorption by SiS/PVA-GO are given in Table 5. As the liquid mass transfer is directly proportional to the flow rate, which means that lower mass transfer resistance works at a higher flow rate and vice-versa, therefore, the k_{TH} increases with a rise in flow rate. Similarly, the q_o increases with increasing initial concentration and flow rate might be due to the existence of higher mass-transfer forces and the involvement of the surface complexation mechanism[57,61]. Furthermore, mass-transfer resistance grows with bed height resulting in a drop of k_{TH} with a rise in bed height. The presence of high correlation coefficients $R^2 > 0.993$ at all examined conditions shows a better fit.

3.4.2. Yoon-Nelson Model

This model was established to examine the vapour and gas adsorption onto activated charcoal. However, it was later used in a fixed-bed column to forecast pollutant behaviour during adsorption[65]. This model assumes that the possibility of adsorbate breakthroughs on the adsorbent and adsorbate adsorption is inversely related to the probability of t adsorption rate[65]. It assumes that there's no axial dispersion or external mass transfer resistance. The breakthrough rate and time of 50% could be obtained using the following equation, i.e., Eqs. 11.

$$\frac{C_t}{C_o}=\frac{1}{1+\exp(k_{YN}*(\tau-t))} \quad (11)$$

where k_{YN} (1/min) stands for the rate constant, and τ (min) denotes the time when the effluent concentration reaches 50% of its influent concentration.

The obtained model fitting parameters are presented in Table 5, and the non-linear plots at different conditions are shown in Figure 6.1 d-f. The increase in k_{YN} with initial Cd^{2+} concentration might be due to the high mass transfer achieved in the column. Similarly, the drop in 'τ' with a rise in the initial concentration specifies that the column saturated quickly due to higher Cd^{2+} loading. Additionally, the surge in 'τ' with the rise in bed height further shows that the abundant SiS/PVA-GO in bed leads to a slow saturation column. The Y-N model fits with high R^2 on the experimental data and adequately correlates experimental and predicted values.

3.4.3. Bed Depth Service Time (BDST) Model

The BDST is an improved and modified version of the Adams-Bohart model, which enables us to forecast the breakthrough time at 5% and 85% breakthrough[15,66].

The BDST model assumes that there is a linear relationship between the bed depth and the time it takes for the breakthrough to occur at a particular concentration. It is mostly useful in predicting scale-up parameters. The model assumes that the moving bed speed of the adsorption zone in the column stays constant and considers the surface interaction between the unused adsorbent capacity and the mass concentration of the adsorbent. Internal diffusion resistance and mass transfer that take place during the process are not counted. Its non-linear equation can be presented in Eqs.12.

$$\frac{C_t}{C_o}=\frac{1}{1+\exp(k_{BDST}*Co\left(\frac{No}{Co*v}*L-t\right))} \quad (12)$$

Where k_{BDST} (L/mg.min) is liquid to solid phase mass-transfer rate. N_o (mg/L) and L (cm) is the fixed-bed adsorption capacity fixed-bed height. 'v' is the linear flow velocity in mL/min.

The experimental data collected under various column conditions were fit using the non-linear correlation, and the constants from the model fitting are presented in Table 5, along with the pertinent graphs in Figure 6.2 (g, h, and i). The higher R^2 value (>0.98) at all the column conditions depicting the adsorption of Cd^{2+} onto SiS/PVA-GO can be best described using this model. Further, k_{BDST} increases with the rise in the flow rate but declines when the initial Cd^{2+} concentration increases, depicting a higher Cd^{2+} adsorption rate. As the adsorbent approaches the breakthrough point or towards saturation, the adsorption rate decreases considerably. The highest N_o and lowest k_{BDST} were observed at the highest bed height revealing the optimum condition for column use. Also, the other values obtained from this BDST model fitting would open the scope for upscaling the SiS/PVA-GO-based material filter.

3.4.4. Dose-Response (D-R) Model

The D-R model is used to explain the adsorption of metal onto a solid surface[67]. The D-R model is used to predict breakthrough curves in the initial adsorption phases. The D-R model assumes that the probability of response increases with dose and so gives a good understanding of the sorption mechanism. Table 5 presents the parameters obtained from the D-R model fitting, and the respective non-linear plot is shown in Figure 6.2 (j, k, and l). The non-linear D-R model equation[15] is produced in Eqs. 13.

$$\frac{C_t}{C_o}=1-\frac{1}{1+\left(\frac{Co*Q*t}{qo*X}\right)^a} \quad (13)$$

Where 'a' is constant, all other terms have the same meaning as above, and 'X' (mg) is the adsorbent mass.

The D-R model fits well with the experimental data with R^2 value >0.993 in all column conditions. The adsorption capacity (q_o (g/L)) decreases with the surge in the flow-rate, which can be accredited to reducing interaction between Cd^{2+} and the SiS/PVA-GO. However, the 'q_o' elevate with increased bed-height and initial Cd^{2+} concentration.

The models used have their advantages and limitations. For example, the Thomas and Yoon-Nelson models are usually more useful for continuous systems and the D_R model is more relevant for batch systems. However, in study design and adsorptive media comparison, the BDST model might provide more straightforward comparison standards. Therefore, for real applications, all these models are important since no one model is versatile for all different situations observed in practice. Hence, combining these specific models with pilot or bench studies is often necessary for a more accurate prediction.

3.5. Adsorption Mechanism

The importance of accessing the Cd^{2+} interaction with SiS/PVA-GO helps to improve the material efficiency and design Cd^{2+} or similar heavy metals contaminated water purification systems. The interaction among the oxygenic groups of GO-based adsorbents and heavy metals is complex and commonly involves ion exchange, surface complexation, physical adsorption, and electrostatic interaction[9,68]. The batch and column experiments seldom provide sufficient information to explain the interaction mechanism. Therefore, in the present study SEM, EDS, and XPS analysis of the Cd^{2+} adsorbed SiS/PVA-GO samples was performed for a detailed investigation of the adsorption mechanism. The existence of tiny white patches on the surface and interiors was observed in SEM images of spent SiS/PVA-GO (Figure 7a) and could be attributed to the presence of $CdCO_3$ onto the SiS/PVA/GO surface, indicating the involvement of physical adsorption[69]. Furthermore, the EDS examination of Cd^{2+} adsorbed SiS/PVA-GO surface (Figures 7a and 7b) reveals the presence of Si, O, C, and Cd in 53.99, 23.17, 19.34, and

Table 5. Parameters of non-linear fitting of the Thomas, Yoon-Nelson, BDST, and D-R models at the various flow rate (Q), bed height (Z), and initial influent concentration (C_o)(Experimental condition: pH = 8.8±0.3, Temperature = 25±3 °C)

Column parameters					Thomas model parameters			Yoon Nelson parameters		
C_o (mg/L)	Z (cm)	W (g)	$\chi^2 * 10^{-4}$	Q (mL/min)	K_{TH} (mL/mgmin^{-1})	q_o (mg/g)	R^2	K_{YN} (1/min)	τ (min)	R^2
20	5	5.0	2.3	5	0.0207	267.07	0.998	0.0236	269.7	0.988
20	5	5.0	11	10	0.0311	133.53	0.993	0.0376	148.07	0.984
20	5	5.0	21	15	0.0396	86.24	0.968	0.0478	101.01	0.978
20	10	10.5	4.4	10	0.0210	282.23	0.996	0.0208	288.30	0.987
20	15	15.0	1.2	10	0.0192	439.78	0.999	0.0156	446.77	0.989
10	5	5	7.8	10	0.0256	201.66	0.995	0.0294	224.85	0.985
30	5	5	22	10	0.0370	94.28	0.987	0.0442	117.11	0.977
Column parameters					**Bed depth-service time (BDST) model**			**Dose-Response model**		
C_o (mg/L)	Z (cm)	W (g)	$\chi^2 * 10^{-4}$	Q (mL/min)	K_{BDST} (mL/mg×min)	No (g/L)	R^2	q_o (g/L)	a	R^2
20	5	5.0	2.3	5	0.00104	6761	0.997	5322	5.45	0.994
20	5	5.0	11	10	0.00155	6761	0.997	5079	3.89	0.994
20	5	5.0	21	15	0.00198	6550	0.985	4722	3.05	0.993
20	10	10.5	4.4	10	0.00105	7145	0.995	5272	5.86	0.997
20	15	15.0	1.2	10	0.000958	7423	0.998	5811	8.38	0.999
10	5	5.0	7.8	10	0.00256	5106	0.994	3932	4.99	0.999
30	5	5.0	22	10	0.00123	7161	0.986	5200	3.05	0.996

Where, C_o (mg/L) = initial Concentration, C_t = Concentration at a time 't'. q_o = adsorption capacity. t = adsorption time. v and Q are the flow rates in a column. W and X are the weights of the adsorbent. τ = time for 50% adsorbate breakthrough. k_{TH}, k_{YN} are the rate constant, k_{BDST} = rate of mass transfer. N_o = adsorption capacity of bed, L and Z = bed heights.

3.50%, respectively. The presence of Cd throughout the SiS/PVA-GO surface reveals the occurrence of adsorption sites all over the adsorbent surface. Besides, the XPS scan spectra (Figure 7c) again displayed the existence of Si, O, C, and Cd in a proportion of 69.8, 27.2, 2.8, and 0.2%, respectively, reiterating the SEM (EDS) observation. Additionally, the deconvolution of C1s (Figure 7d) and Si2p (Figure 7e) spectra of spent adsorbent (Cd^{2+} adsorbed SiS/PVA-GO) spectra gave rise to peaks at 285.3 and 286.8 eV are of C-O and C=O/O-C-O; while peaks at 102.4, and 103.2 eV represent Si-O/Si-O-C and SiO_2, respectively. This result shows that the integrity of the material was intact during the adsorption process. However, the deconvolution of Cd 3d spectra (Figure 7f) revealed the presence of peaks at 406.1 and 412.8 eV, which could be allocated to Cd 3d3/2 and 3d5/2, respectively[70-72]. The shift in C-O and C=O peaks from their original position in the deconvoluted C1s spectra could be due to the involvement of electrostatic attraction between Cd^{2+} and the oxygenic groups of the adsorbent[68,69]. Moreover, the adoption of Cd^{2+} onto the SiS/PVA-GO surface could also be through an ion-exchange mechanism (Bian, Yu, *et al.* 2015), which may be explained with the help of the following Eqs. 12 to 15.

$$-COOH + Cd^{2+} \rightarrow -COOCd^{+} + H^{+} \quad (12)$$

$$-2COOH + Cd^{2+} \rightarrow -COOCdOOC + 2H^{+} \quad (13)$$

$$-OH + Cd^{2+} \rightarrow -OCd^{+} + H^{+} \quad (14)$$

$$-2OH + Cd^{2+} \rightarrow -OCdO + 2H^{+} \quad (15)$$

Hence, based on the above analysis, it was inferred that the adsorption of Cd^{2+} by SiS/PVA-GO involved mainly physical adsorption, electrostatic interaction, and ion exchange. However, other molecular interaction mechanisms, e.g., H-bonding, cation-π, and

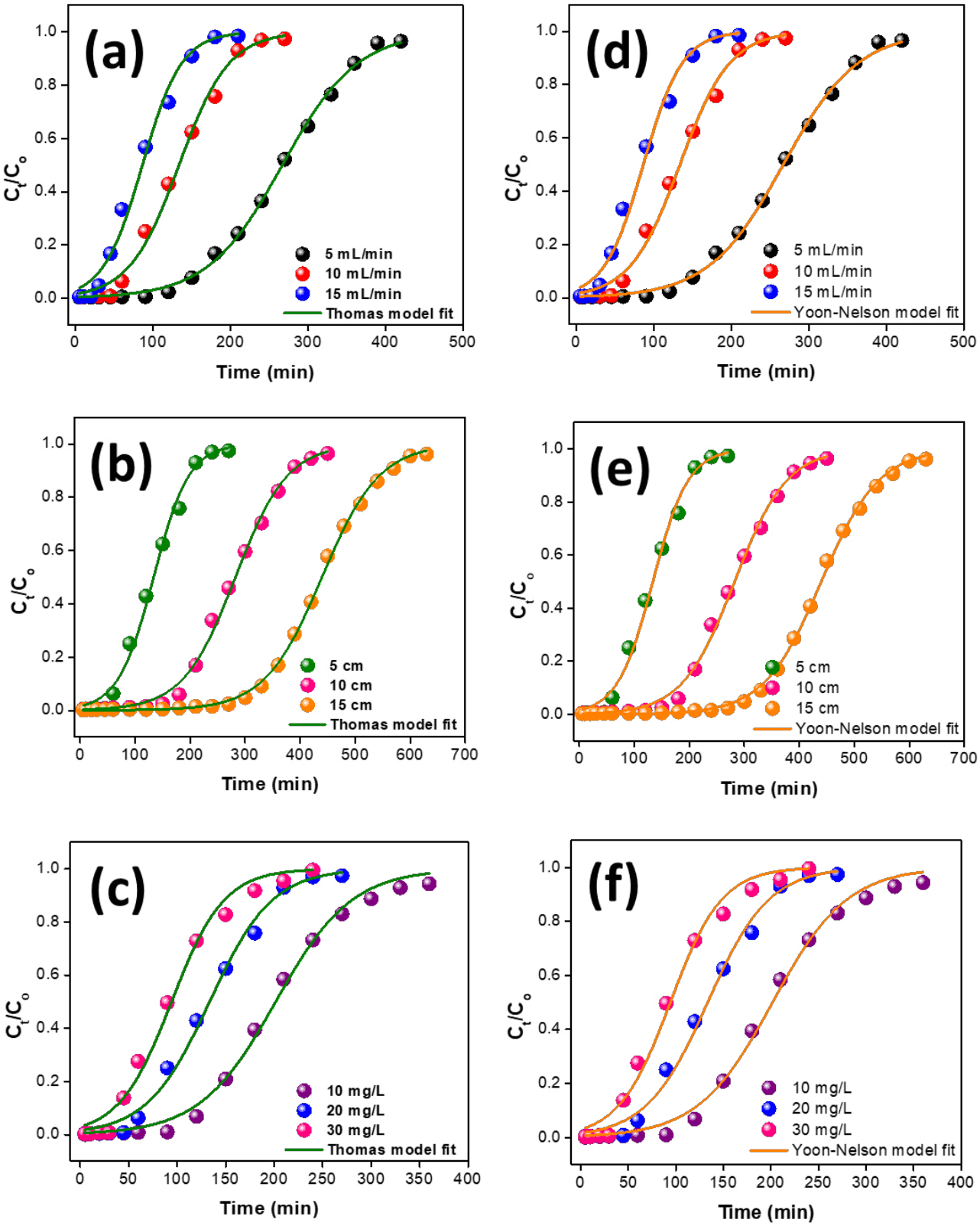


Figure 6.1. Non-linear model fitting of the Thomas (a, b, and c), Yoon-Nelson model (d, e, and f) at different flow rates, bed height, and initial concentrations.

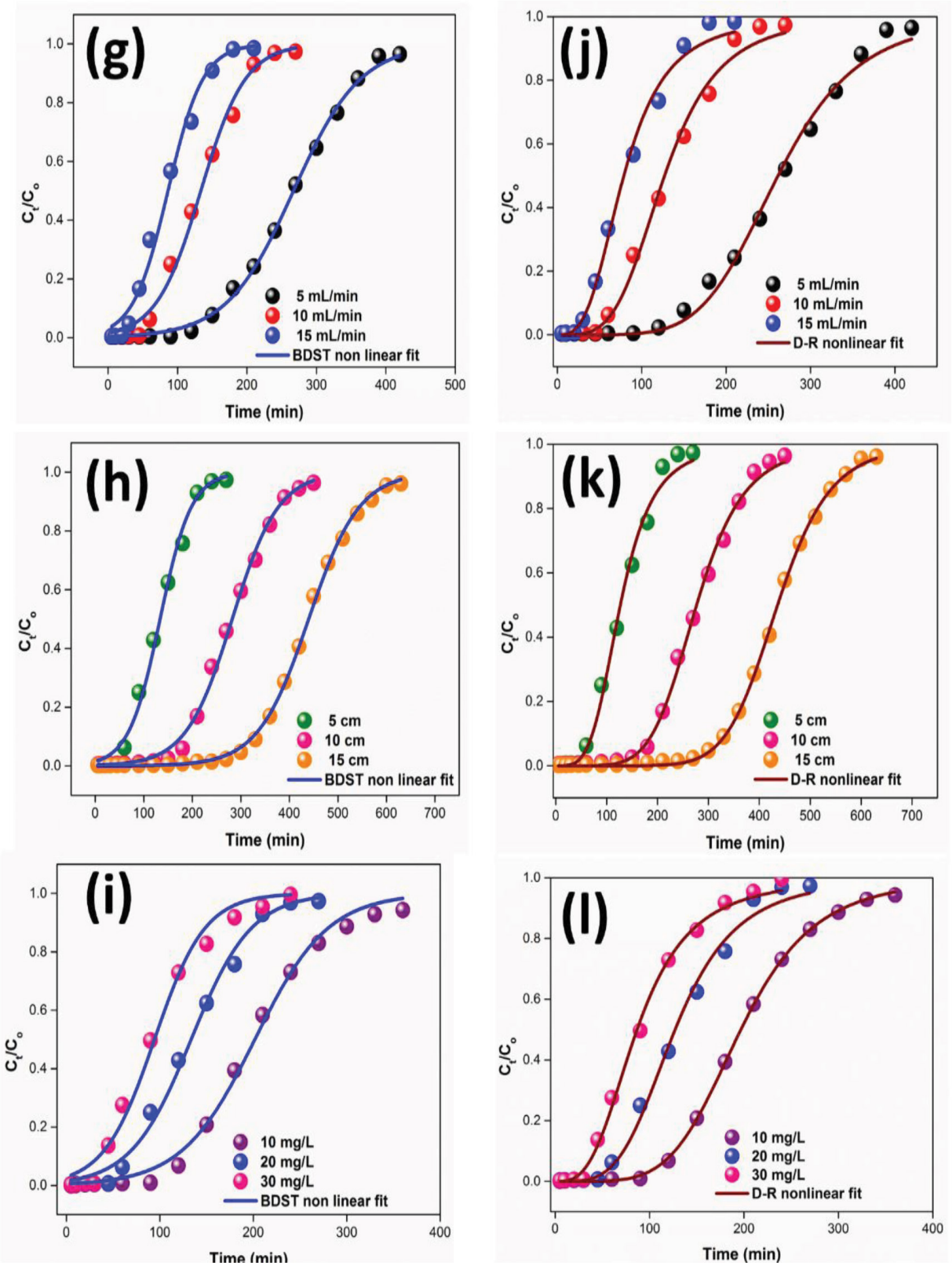


Figure 6.2. Non-linear model fitting of the BDST model (g, h, and i) and D-R Model (j, k, and l) at different flow rates, bed heights and Initial concentrations.

complexation, cannot be neglected. An illustration of the possible mechanism of Cd^{2+} sorption is provided in Figure 8, which is like the previous one reported by Bian *et al.* 2015, Park *et al.* 2019, Chaabane *et al.* 2020, and Rout *et al.* 2023atomic force microscopy (AFM[73-76]).

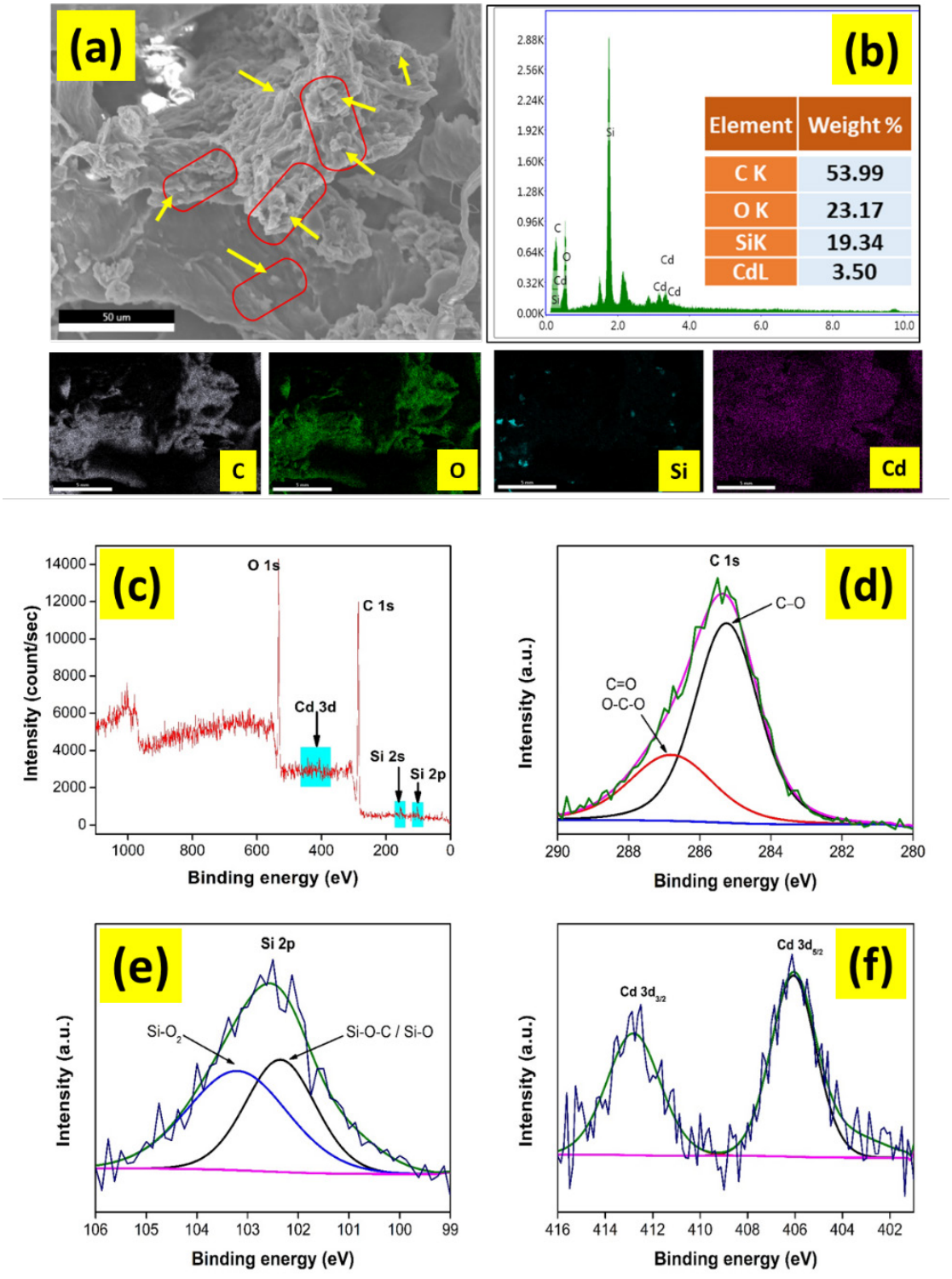


Figure 7. Post adsorption characterization of SiS/PVA-GO (a) Micrograph obtained from SEM, (b) EDS spectra and elemental mapping representing C, O, Si, and Cd; (c) XPS scan spectra, (d) XPS deconvoluted C1s spectra, (e) Si 2p, and (f) Cd 3d spectra.

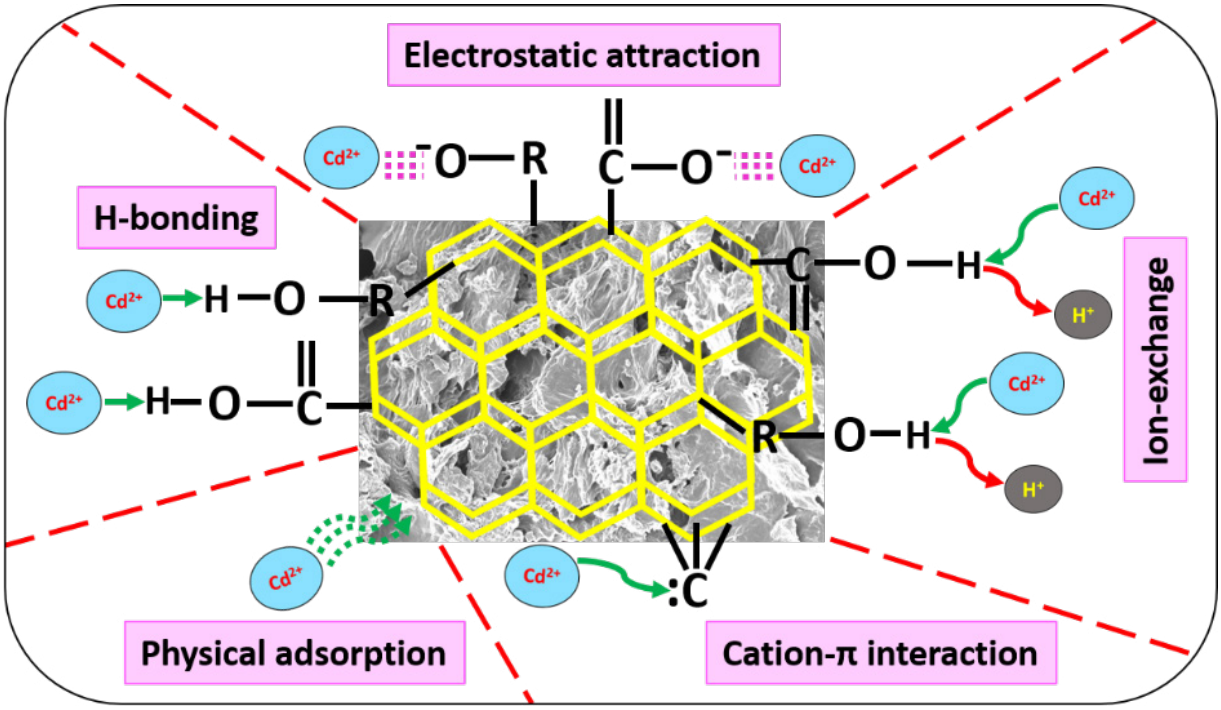


Figure 8. Mechanistic illustration of the adsorption mechanism of Cd^{2+} by SiS/PVA-GO.

4.0 Conclusion

The long-term sustainability of the ecosystem is gravely threatened by water contamination. Therefore, an effort is directed toward novel GO-based composite development for efficient and cost-effective wastewater treatment. This study successfully developed a trio-composite of Silica sand, GO, and PVA (SiS/PVA-GO) without using harmful chemicals. The SiS/PVA-GO characterization using FESEM, FTIR, XPS, and XRD revealed the formation of interconnected pores for easy access to the sorption sites and smooth water transport during the adsorption process. Moreover, the batch adsorption test discloses rapid Cd^{2+} adsorption by attaining equilibrium in ≤ 30 min and following the PSO kinetics model. In a batch study, the Freundlich adsorption isotherm model provided the best fit and demonstrated a maximum sorption capacity of 3.7 mg/g.

Furthermore, the column performance varied significantly with changes in bed height, flow rate, and initial concentration, showing the highest Cd^{2+} adsorption at 5.8 mg/g. The dynamic modelling of the breakthrough curve and fitting of nonlinear models (the Thomas, Yoon-Nelson, BDST, and D-R models) revealed a good correlation with the experimental data. The post-adsorbed composite characterization suggests that electrostatic attraction, cation-π interaction, and ion exchange are the predominant forces responsible for Cd^{2+} adsorption onto SiS/PVA/GO. This work provides unique insight into designing and upscaling GO-enabled systems for the rapid purification of heavy metal-contaminated water. Future research is still required via examining single and multiple variables while taking into account the complex characteristics of real wastewater for a better understanding and scale-up design, as well as evaluating the composite's life cycle assessment to ensure the sustainability of the adsorbent material.

Supplementary Information

S1. Instrumental Characterization

The microstructure of SiS/PVA-GO was inspected using a Field Emission Scanning Electron Microscope (FESEM) on the Carl-Zeiss MERLIN FESEM model no. GEMINI-2 and the elemental presence and distribution were determined using Energy-Dispersive X-ray Spectroscopy (EDS) elemental mapping. The surface topography of GO and GO-PVA was studied using Atomic Force Microscopy (AFM) of Agilent Technologies' model 5500 in tapping mode. The GO-PVA liquid sample was spin-coated on the substrate (silicon wafers) for AFM analysis.

X-ray diffraction (XRD) patterns were collected between 2θ = 5 to 50° (Cu Kα radiation at λ = 1.540 Å), model no. X`pert powder of PAN analytical. The functional groups present on the surface were determined by a Fourier Transform Infrared (FTIR) spectrophotometer (Thermo Fisher, model no. Nicolet 6700) by scanning the sample between 400-4000 cm^{-1} range. Brunauer–Emmett–Teller (BET) analysis was conducted on model AUTOSORB-1 Quantachrome Instruments, Florida, USA, to determine the surface area, pore size, and volume of the composite by measuring N_2 adsorption-desorption at -196°C. The BET samples (100 mg) were degassed at 100°C for 5 hours. X-ray Photoelectron Spectroscopy (XPS) of the Cd^{2+} adsorbed sample was performed on PHI 5000 Versa Probe II (ULVAC–PHI, INC, Japan).

S2. Batch Adsorption Study and Theory

Batch adsorption tests were performed in a 125 mL polypropylene (PPP) bottle containing 50 to 550 mg SiS/PVA/GO in 50 mL Cd^{2+} solution (10 to 50 mg/L) at pH ranging from 2.0 to 8.8. The sealed bottles containing SiS/PVA/GO and Cd^{2+} solution were agitated at 180 rpm in an incubator shaker at different temperatures (30 to 50°C). To examine the effect of pH, adsorbent dose, and adsorbate concentration, a series of experiments were performed by varying a single parameter and keeping the others constant. The samples were collected at a certain interval followed by filtration using a 0.22 µm pore size filter to remove adsorbent and then analyzing the remaining Cd^{2+} concentration in the solution by Atomic Absorption Spectrophotometer (AAS) Thermo Scientific, model- iCE3300. The batch adsorption kinetics was studied at three initial concentrations (C_o) = 10, 20, and 50 mg/L. The adsorption isotherm was performed at three temperatures i.e., 30, 40, and 50°C, by fixing the adsorbate (Cd^{2+}) concentration to 20 mg/L and varying the dose of SiS/PVA/GO from 1.0 to 11.0 g/L.

S3.1. Calculations

The percentage removal (%R) of Cd^{2+} was calculated using Eq. S1:

$$\%R = \frac{C_o - C_e}{C_o} \times 100 \quad \text{(S1)}$$

The amount of Cd^{2+} adsorbed per unit of adsorbent at time t (q_t) and at equilibrium condition (q_e) was determined using the following equations:

$$q_t = \frac{C_o - C_t}{W} \times V \quad \text{(S2)}$$

$$q_e = \frac{C_o - C_e}{W} \times V \quad \text{(S3)}$$

Where, C_o, C_t, and C_e are the Cd^{2+} concentration (mg/L) at t = 0, t, and equilibrium, respectively. Whereas, q_e and q_t are SiS/PVA/GO adsorption capacity (mg/g) at equilibrium and time t. V (mL) volume of Cd^{2+} solution and W (g) is the SiS/PVA/GO weight for a particular study.

S3.2. Batch Adsorption Kinetics

The three kinetic models namely the pseudo-first-order[1], pseudo-second-order[2], and Elovich (Eqs. S6) were tested to fit the experimental data. Furthermore, insights into the Cd^{2+} adsorption were assessed by fitting the experimental sorption data to the intraparticle diffusion model[3].

$$q_t = q_e\,(1 - e^{-k_1 t})) \quad \text{(S4)}$$

$$q_t = \frac{k_2 q_e^2 t}{1 + k_2 q_e t} \quad \text{(S5)}$$

$$q_t = \frac{1}{\beta}\ln(1 + \alpha\beta t) \quad \text{(S6)}$$

$$q_t = k_{ip}\sqrt{t} + c_i \quad \text{(S7)}$$

where, k_1 (min^{-1}), k_2 (g/mg×min), and k_{ip} ($mg \times g \times min^{0.5}$) are the rate constants of pseudo-first order, pseudo-second order, and intraparticle diffusion models, respectively. Whereas, c is the constant related to boundary layer thickness.

S3.3. Batch Adsorption Isotherm

Three isotherm models namely Langmuir (S8), Freundlich (S9), and Temkin (S10) were applied to fit the experimental data[4,5].

$$q_e = \frac{q_m K_L C_e}{1 + K_L C_e} \quad \text{(S8)}$$

$$q_e = K_F C_e^{1/n} \quad \text{(S9)}$$

$$q_e = \frac{RT}{b_T}\ln A_T C_e \quad \text{(S10)}$$

where q_m is the maximum adsorption capacity (mg/g) of the SiS/PVA/GO. K_L (L/mg), K_F ((mg/g)(L/mg)$^{1/n}$), and b_T (kJ/mol) are the Langmuir, Freundlich, and Temkin

isotherm constants, respectively. The A_T is the Temkin isotherm equilibrium binding constant and n is the heterogeneity factor of the Freundlich isotherm. The other notations have the usual meaning as shown in the above equations.

S4. SiS/PVA/GO Recyclability

A 0.1N HNO_3 solution was used to regenerate the SiS/PVA/GO. After adsorption of Cd^{2+}, the exhausted SiS/PVA/GO was agitated with the 0.1N HNO_3 solution for 30 minutes, before being filtered and rinsed with DI water until a neutral pH was achieved. The regenerated SiS/PVA/GO was then tested for additional cycles of adsorption and desorption. It was observed that the regenerated SiS/PVA/GO could effectively be used for a minimum of four consecutive Cd^{2+} adsorption cycles before the efficiency of the adsorbent fell to 50%. This study enhances the appeal of the SiS/PVA/GO as a potential option for a cost-efficient adsorbent in wastewater treatment.

Figures

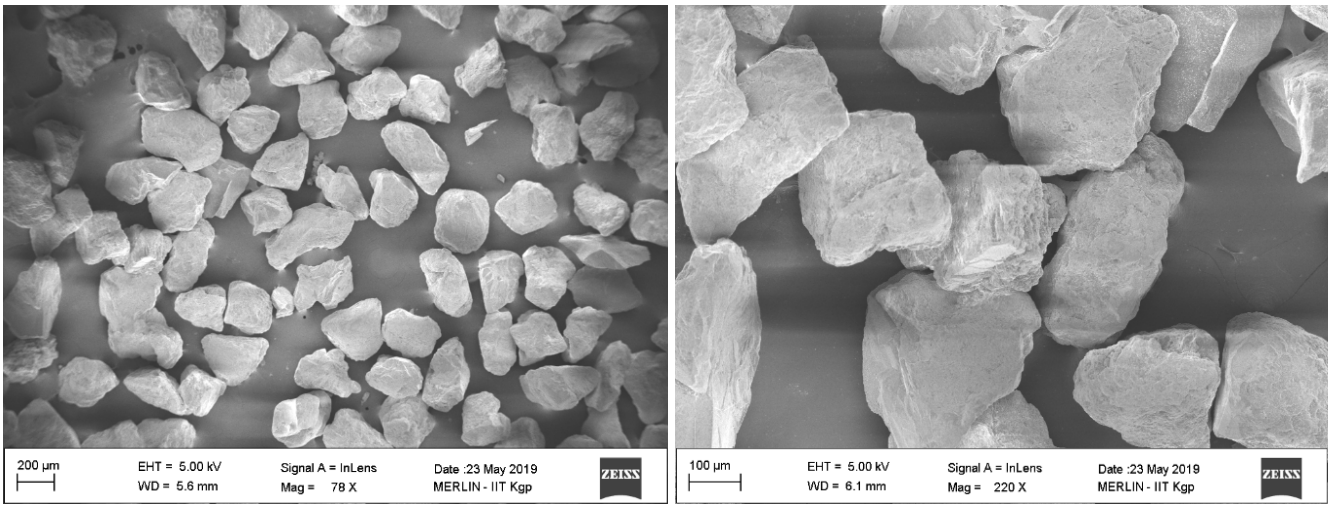


Figure S1. Micrograph of pure sand particles.

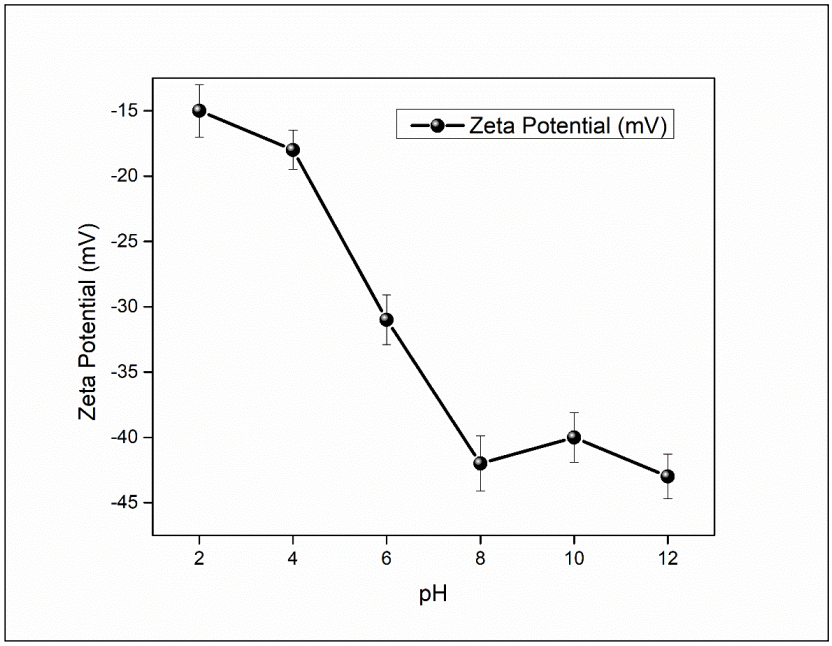


Figure S2. pH vs Zeta Potential graph for SiS/PVA/GO.

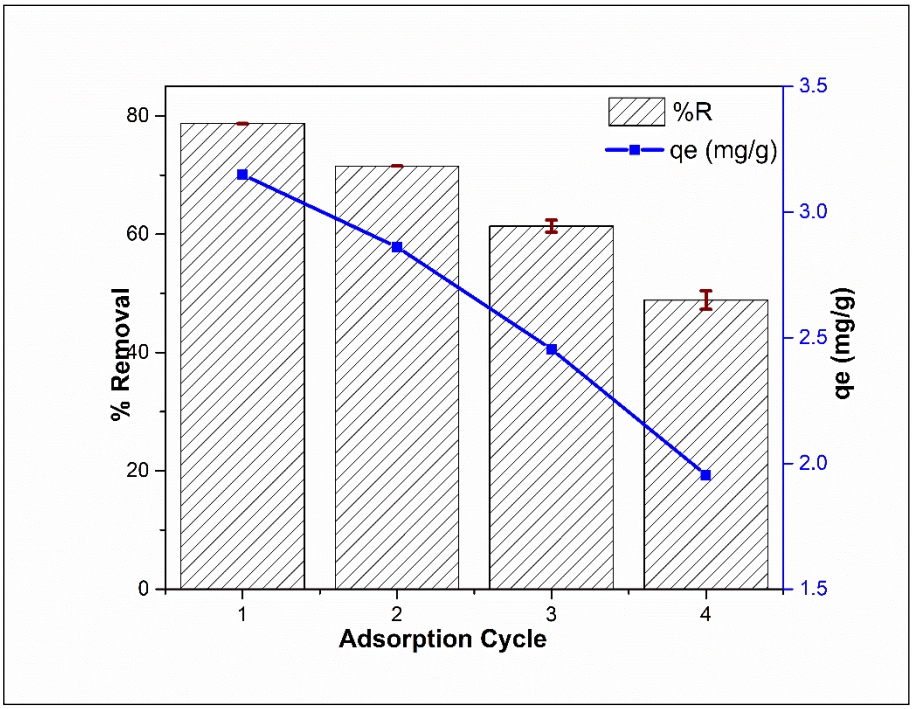


Figure S3. SiS/PVA/GO recyclability.

5.0 References

1. Nag S, Mondal A, Roy DN, Bar N, Das SK. Sustainable bioremediation of Cd (II) from aqueous solution using natural waste materials: kinetics, equilibrium, thermodynamics, toxicity studies and GA-ANN hybrid modelling. Environ Technol Innov. 2018; 11:83-104. https://doi.org/10.1016/j.eti.2018.04.009
2. Rathour RK, Bhattacharya J, Mukherjee A. β-Cyclodextrin conjugated graphene oxide: A regenerative adsorbent for cadmium and methylene blue. J Mol Liq. 2019; 282:606-16. https://doi.org/10.1016/j.molliq.2019.03.020
3. Chandrasekaran B, Dahiya NR, Tyagi A, Kolluru V, Saran U, Baby BV, *et al.* Chronic exposure to cadmium induces a malignant transformation of benign prostate epithelial cells. Oncogenesis. 2020; 9(2):23. https://doi.org/10.1038/s41389-020-0202-7
4. Zang Y, Devleesschauwer B, Bolger PM, Goodman E, Gibb HJ. Global burden of late-stage chronic kidney disease resulting from dietary exposure to cadmium, 2015. Environ Res. 2019; 169:72-8. https://doi.org/10.1016/j.envres.2018.10.005
5. Kubier A, Wilkin RT, Pichler T. Cadmium in soils and groundwater: A review. Appl Geochem. 2019; 108:104388. https://doi.org/10.1016/j.apgeochem.2019.104388
6. Bolisetty S, Peydayesh M, Mezzenga R. Sustainable technologies for water purification from heavy metals: review and analysis. Chem Soc Rev. 2019; 48(2):463-87. https://doi.org/10.1039/C8CS00493E
7. Carolin CF, Kumar PS, Saravanan A, Joshiba GJ, Naushad M. Efficient techniques for the removal of toxic heavy metals from the aquatic environment: A review. J Environ Chem Eng. 2017; 5(3):2782-99. https://doi.org/10.1016/j.jece.2017.05.029
8. Vardhan KH, Kumar PS, Panda RC. A review on heavy metal pollution, toxicity and remedial measures: Current trends and future perspectives. J Mol Liq. 2019; 290:111197. https://doi.org/10.1016/j.molliq.2019.111197
9. Duan C, Ma T, Wang J, Zhou Y. Removal of heavy metals from aqueous solution using carbon-based adsorbents: A review. J Water Process Eng. 2020; 37:101339. https://doi.org/10.1016/j.jwpe.2020.101339
10. Singh H, Rathour RK, Raj S, Bhattacharya J. Facile synthesis of gC3N4/MoS2 composite for rapid sequestration of lead and methylene blue and its potential application in paint industry wastewater remediation. Environ Nanotechnol Monit Manag. 2023; 19:100777. https://doi.org/10.1016/j.enmm.2023.100777
11. Wu W, Taipabu MI, Chang WC, Viswanathan K, Xie YL, Kuo PC. Economic dispatch of torrefied biomass polygene-ration systems considering power/SNG grid demands. Renew Energy. 2022; 196:707-19. https://doi.org/10.1016/j.renene.2022.07.007

12. Taipabu MI, Viswanathan K, Chen HT, Wu W. Green solvent production of ethyl lactate via process intensification. J Taiwan Inst Chem Eng. 2023; 146:104876. https://doi.org/10.1016/j.jtice.2023.104876
13. Auta M, Hameed BH. Chitosan-clay composite is a highly effective and low-cost adsorbent for batch and fixed-bed adsorption of methylene blue. Chem Eng J. 2014; 237:352-61. https://doi.org/10.1016/j.cej.2013.09.066
14. Dichiara AB, Weinstein SJ, Rogers RE. On the choice of batch or fixed bed adsorption processes for wastewater treatment. Ind Eng Chem Res. 2015; 54(34):8579-86. https://doi.org/10.1021/acs.iecr.5b02350
15. Singh H, Raj S, Rathour RK, Bhattacharya J. Bimetallic Fe/Al-MOF for the adsorptive removal of multiple dyes: optimization and modelling of batch and hybrid adsorbent-river sand column study and its application in textile industry wastewater. Environ Sci Pollut Res. 2022; 29(37):56249-64. https://doi.org/10.1007/s11356-022-19686-x
16. Zang Y, Devleesschauwer B, Bolger PM, Goodman E, Gibb HJ. Global burden of late-stage chronic kidney disease resulting from dietary exposure to cadmium, 2015. Environ Res. 2019; 169:72-8. https://doi.org/10.1016/j.envres.2018.10.005
17. Nagar A, Pradeep T. Clean water through nanotechnology: needs, gaps, and fulfilment. ACS Nano. 2020; 14(6):6420-35. https://doi.org/10.1021/acsnano.9b01730
18. Falinski MM, Turley RS, Kidd J, Lounsbury AW, Lanzarini-Lopes M, Backhaus A, *et al.* Doing nano-enabled water treatment right: sustainability considerations from design and research through development and implementation. Environ Sci Nano. 2020; 7(11):3255-78. https://doi.org/10.1039/D0EN00584C
19. Mauter MS, Zucker I, Perreault F, Werber JR, Kim JH, Elimelech M. The role of nanotechnology in tackling global water challenges. Nat Sustain. 2018; 1(4):166-75. https://doi.org/10.1038/s41893-018-0046-8
20. Ahmad SZ, Salleh WN, Ismail AF, Yusof N, Yusop MZ, Aziz F. Adsorptive removal of heavy metal ions using graphene-based nanomaterials: Toxicity, roles of functional groups and mechanisms. Chemosphere. 2020; 248:126008. https://doi.org/10.1016/j.chemosphere.2020.126008
21. Liu X, Ma R, Wang X, Ma Y, Yang Y, Zhuang L, *et al.* Graphene oxide-based materials for efficient removal of heavy metal ions from aqueous solution: A review. Environ Pollut. 2019; 252:62-73. https://doi.org/10.1016/j.envpol.2019.05.050
22. Rathour RK, Singh H, Bhattacharya J, Mukherjee A. Sand coated with graphene oxide-PVA matrix for aqueous Pb2+ adsorption: Insights from optimization and modelling of batch and continuous flow studies. Surf Interfaces. 2022; 32:102115. https://doi.org/10.1016/j.surfin.2022.102115
23. Zhao J, Wang Z, White JC, Xing B. Graphene in the aquatic environment: adsorption, dispersion, toxicity and transformation. Environ Sci Technol. 2014; 48(17):9995-10009. https://doi.org/10.1021/es5022679
24. Yousefi N, Lu X, Elimelech M, Tufenkji N. Environmental performance of graphene-based 3D macrostructures. Nat Nanotechnol. 2019; 14(2):107-19. https://doi.org/10.1038/s41565-018-0325-6
25. Ma Z, Liu D, Zhu Y, Li Z, Li Z, Tian H, *et al.* Graphene oxide/chitin nanofibril composite foams as column adsorbents for aqueous pollutants. Carbohydr Polym. 2016; 144:230-7. https://doi.org/10.1016/j.carbpol.2016.02.057
26. Kumar P, Cledon M, Brar SK. A low-cost graphitized sand filter to deliver MC-LR-free potable water: Water treatment plants and household perspective. Sci Total Environ. 2020; 747:141135. https://doi.org/10.1016/j.scitotenv.2020.141135
27. Gao W, Majumder M, Alemany LB, Narayanan TN, Ibarra MA, Pradhan BK, *et al.* Engineered graphite oxide materials for application in water purification. ACS Appl Mater Interfaces. 2011; 3(6):1821-6. https://doi.org/10.1021/am200300u
28. Gong JL, Zhang YL, Jiang Y, Zeng GM, Cui ZH, Liu K, *et al.* Continuous adsorption of Pb(II) and methylene blue by engineered graphite oxide-coated sand in a fixed-bed column. Appl Surf Sci. 2015; 330:148-57. https://doi.org/10.1016/j.apsusc.2014.11.068
29. Hou W, Zhang Y, Liu T, Lu H, He L. Graphene oxide coated quartz sand as a high-performance adsorption material in the application of water treatment. RSC Adv. 2015; 5(11):8037-43. https://doi.org/10.1039/C4RA11430B
30. Li X, Liu T, Wang D, Li Q, Liu Z, Li N, *et al.* Superlight adsorbent sponges based on graphene oxide cross-linked with poly(vinyl alcohol) for continuous flow adsorption. ACS Appl Mater Interfaces. 2018; 10(25):21672-80. https://doi.org/10.1021/acsami.8b06802
31. Chen Y, Yang L, Xu S, Han S, Chu S, Wang Z, *et al.* Ultralight aerogel based on molecular-modified poly (m-phenylenediamine) crosslinking with polyvinyl alcohol/graphene oxide for flow adsorption. RSC

Adv. 2019; 9(40):22950-6. https://doi.org/10.1039/C9RA04207E
32. Marcano DC, Kosynkin DV, Berlin JM, Sinitskii A, Sun Z, Slesarev A, *et al.* Improved synthesis of graphene oxide. ACS Nano. 2010; 4(8):4806-14. https://doi.org/10.1021/nn1006368
33. Rathour RK, Bhattacharya J. A green approach for single-pot synthesis of graphene oxide and its composite with Mn3O4. Appl Surf Sci. 2018; 437:41-50. https://doi.org/10.1016/j.apsusc.2017.12.139
34. Han C, Meng Q, Cao B, Tian G. Enhanced hybrid capacitive deionization performance by sodium titanium phosphate/reduced porous graphene oxide composites. ACS Omega. 2019; 4(7):11455-63. https://doi.org/10.1021/acsomega.9b00984
35. Zhang X, Zhou Y, Zhang J. *In-situ* reduced graphene oxide-polyvinyl alcohol composite coatings as protective layers on magnesium substrates. Prog Nat Sci Mater Int. 2017; 27(3):326-8. https://doi.org/10.1016/j.pnsc.2017.04.016
36. Dave HK, Nath K. Graphene oxide incorporated novel polyvinyl alcohol composite membrane for pervaporation recovery of acetic acid from vinegar wastewater. J Water Process Eng. 2016; 14:124-34. https://doi.org/10.1016/j.jwpe.2016.11.002
37. Rathour R, Das P, Aikat K. Microwave-assisted synthesis of graphene and its application for adsorptive removal of malachite green: thermodynamics, kinetics and isotherm study. Desalin Water Treat. 2016; 57(16):7312-21. https://doi.org/10.1080/19443994.2015.1020507
38. Rathour RK, Bhattacharya J, Mukherjee A. Selective and multicycle removal of Cr(VI) by graphene oxide-EDTA composite: insight into the removal mechanism and ionic interference in binary and ternary associations. Environ Technol Innov. 2020; 19:100851. https://doi.org/10.1016/j.eti.2020.100851
39. Lee JS, Choi KH, Ghim HD, Kim SS, Chun DH, Kim HY, et al. Role of molecular weight of atactic poly (vinyl alcohol) (PVA) in the structure and properties of PVA nanofabric prepared by electrospinning. J Appl Polym Sci. 2004; 93(4):1638-46. https://doi.org/10.1002/app.20602
40. Badr YA, Abd El-Kader KM, Khafagy RM. Raman spectroscopic study of CdS, PVA composite films. J Appl Polym Sci. 2004; 92(3):1984-92. https://doi.org/10.1002/app.20017
41. Bao C, Guo Y, Song L, Hu Y. Poly (vinyl alcohol) nanocomposites based on graphene and graphite oxide: a comparative investigation of property and mechanism. J Mater Chem. 2011; 21(36):13942-50. https://doi.org/10.1039/c1jm11662b
42. Ricciardi R, Auriemma F, De Rosa C, Lauprêtre F. X-ray diffraction analysis of poly (vinyl alcohol) hydrogels, obtained by freezing and thawing techniques. Macromolecules. 2004; 37(5):1921-7. https://doi.org/10.1021/ma035663q
43. Mechri ML, Chihi S, Mahdadi N, Beddiaf S. Study of heat effect on the composition of dunes sand of Ouargla (Algeria) using XRD and FTIR. Silicon. 2017; 9(6):933-41. https://doi.org/10.1007/s12633-015-9368-6
44. Anbalagan G, Prabakaran AR, Gunasekaran S. Spectroscopic characterization of Indian standard sand. J Appl Spectrosc. 2010; 77:86-94. https://doi.org/10.1007/s10812-010-9297-5
45. Pak SY, Huang ZM, Youn JR, Song YS. Morphology and physical properties of graphene nanoplatelet embedded poly (vinyl alcohol) composite aerogel. Curr Appl Phys. 2017; 17(5):727-31. https://doi.org/10.1016/j.cap.2017.02.006
46. Aljerf L. High-efficiency extraction of bromocresol purple dye and heavy metals as chromium from industrial effluent by adsorption onto a modified surface of zeolite: kinetics and equilibrium study. J Environ Manage. 2018; 225:120-32. https://doi.org/10.1016/j.jenvman.2018.07.048
47. Hu XJ, Liu YG, Zeng GM, Wang H, Hu X, Chen AW, *et al.* Effect of aniline on cadmium adsorption by sulfanilic acid-grafted magnetic graphene oxide sheets. J Colloid Interface Sci. 2014; 426:213-20. https://doi.org/10.1016/j.jcis.2014.04.016
48. Hasanpour M, Hatami M. Application of three-dimensional porous aerogels as adsorbent for removal of heavy metal ions from water/wastewater: A review study. Adv Colloid Interface Sci. 2020; 284:102247. https://doi.org/10.1016/j.cis.2020.102247
49. Khan ZH, Gao M, Qiu W, Islam MS, Song Z. Mechanisms for cadmium adsorption by magnetic biochar composites in an aqueous solution. Chemosphere. 2020; 246:125701. https://doi.org/10.1016/j.chemosphere.2019.125701
50. Salawudeen AO, Tawabini BS, Al-Shaibani AM, Saleh TA. Poly (2-hydroxyethyl methacrylate) grafted graphene oxide for cadmium removal from water with interaction mechanisms. Environ Nanotechnol Monit Manage. 2020; 13:100288. https://doi.org/10.1016/j.enmm.2020.100288
51. Medina RP, Nadres ET, Ballesteros FC, Rodrigues DF. Incorporation of graphene oxide into a chitosan-poly (acrylic acid) porous polymer nanocomposite for

enhanced lead adsorption. Environ Sci Nano. 2016; 3(3):638-46. https://doi.org/10.1039/C6EN00021E

52. Kango S, Kumar R. Low-cost magnetic adsorbent for As (III) removal from water: adsorption kinetics and isotherms. Environ Monit Assess. 2016; 188:1-4. https://doi.org/10.1007/s10661-015-5077-2
53. Fan T, Liu Y, Feng B, Zeng G, Yang C, Zhou M, et al. Biosorption of cadmium (II), zinc (II) and lead (II) by *Penicillium simplicissimum*: isotherms, kinetics and thermodynamics. J Hazard Mater. 2008; 160(2-3):655-61. https://doi.org/10.1016/j.jhazmat.2008.03.038
54. Salih SS, Mahdi A, Kadhom M, Ghosh TK. Competitive adsorption of As (III) and As (V) onto chitosan/diatomaceous earth adsorbent. J Environ Chem Eng. 2019; 7(5):103407. https://doi.org/10.1016/j.jece.2019.103407
55. Wang H, Zhou Y, Hu X, Guo Y, Cai X, Liu C, *et al.* Optimization of cadmium adsorption by magnetic graphene oxide using a fractional factorial design. Int J Environ Res Public Health. 2020; 17(18):6648. https://doi.org/10.3390/ijerph17186648
56. Singh Rathour RK, Bhattacharya J, Mukherjee A. Facile synthesis of graphene oxide for multicycle adsorption of aqueous Pb2+ in the presence of divalent cations and polyatomic anions. J Chem Eng Data. 2018; 63(9):3465-74. https://doi.org/10.1021/acs.jced.8b00344
57. Van HT, Nguyen LH, Nguyen XH, Nguyen TH, Nguyen TV, Vigneswaran S, *et al.* Characteristics and mechanisms of cadmium adsorption onto biogenic aragonite shells-derived biosorbent: batch and column studies. J Environ Manage. 2019; 241:535-48. https://doi.org/10.1016/j.jenvman.2018.09.079
58. Rajesh V, Rajesh N. Biosorption study of cadmium, lead and zinc ions onto halophilic bacteria and reduced graphene oxide. J Environ Chem Eng. 2018; 6(4):5053-60. https://doi.org/10.1016/j.jece.2018.07.042
59. Satya A, Harimawan A, Haryani GS, Johir MA, Nguyen LN, Nghiem LD, *et al.* Fixed-bed adsorption performance and empirical modelling of cadmium removal using adsorbent prepared from the cyanobacterium *Aphanothece* sp cultivar. Environ Technol Innov. 2021; 21:101194. https://doi.org/10.1016/j.eti.2020.101194
60. Zhou C, Gong X, Zhang W, Han J, Guo R, Zhu A. Uptake of Cd (II) onto raw crab shells: isotherm, kinetic, adsorption properties and mechanisms. Water Environ Res. 2017; 89(9):817-26. https://doi.org/10.2175/106143017X14902968254854
61. Qu J, Li Y, Zang T, Jin Y, Liu X, Yan L. Removal of Cd (II) ions from aqueous solutions using immobilized spent substrates of *Pleurotus ostreatus* in a fixed-bed column. Environ Eng Sci. 2019; 36(9):1162-9. https://doi.org/10.1089/ees.2019.0088
62. Luo X, Liu F, Deng Z, Lin X. Removal of copper (II) from aqueous solution in a fixed-bed column by carboxylic acid functionalized deacetylated konjac glucomannan. Carbohydr Polym. 2011; 86(2):753-9. https://doi.org/10.1016/j.carbpol.2011.05.020
63. Khalfa L, Sdiri A, Bagane M, Cervera ML. A calcined clay fixed bed adsorption studies for the removal of heavy metals from aqueous solutions. J Clean Prod. 2021; 278:123935. https://doi.org/10.1016/j.jclepro.2020.123935
64. Basu M, Guha AK, Ray L. Adsorption of cadmium ions by cucumber peel in continuous mode. Int J Environ Sci Technol. 2019; 16:237-48. https://doi.org/10.1007/s13762-017-1609-3
65. Cruz-Olivares J, Pérez-Alonso C, Barrera-Díaz C, Ureña-Nuñez F, Chaparro-Mercado MC, Bilyeu B. Modeling of lead (II) biosorption by residue of allspice in a fixed-bed column. Chem Eng J. 2013; 228:21-7. https://doi.org/10.1016/j.cej.2013.04.101
66. Bai S, Li J, Ding W, Chen S, Ya R. Removal of boron by a modified resin in fixed bed column: Breakthrough curve analysis using dynamic adsorption models and artificial neural network model. Chemosphere. 2022; 296:134021. https://doi.org/10.1016/j.chemosphere.2022.134021
67. Shanmugam D, Alagappan M, Rajan RK. Bench-scale packed bed sorption of Cibacron blue F3GA using lucrative algal biomass. Alexandria Eng J. 2016; 55(3):2995-3003. https://doi.org/10.1016/j.aej.2016.05.012
68. Yang X, Wan Y, Zheng Y, He F, Yu Z, Huang J, *et al.* Surface functional groups of carbon-based adsorbents and their roles in the removal of heavy metals from aqueous solutions: a critical review. Chem Eng J. 2019; 366:608-21. https://doi.org/10.1016/j.cej.2019.02.119
69. Xu JC, Ma Q, Chen C, Wu QT, Long XX. Cadmium adsorption behaviour of porous and reduced graphene oxide and its potential for promoting cadmium migration during soil electrokinetic remediation. Chemosphere. 2020; 259:127441. https://doi.org/10.1016/j.chemosphere.2020.127441
70. Kong W, Yue Q, Li Q, Gao B. Adsorption of Cd^{2+} on GO/PAA hydrogel and preliminary recycle to GO/PAA-CdS as efficient photocatalyst. Sci Total Environ. 2019; 668:1165-74. https://doi.org/10.1016/j.scitotenv.2019.03.095

71. Liang X, Xu Y, Sun G, Wang L, Sun Y, Qin X. Preparation, characterization of thiol-functionalized silica and application for sorption of Pb2+ and Cd2+. Colloids Surf A Physicochem Eng Asp. 2009; 349(1-3):61-8. https://doi.org/10.1016/j.colsurfa.2009.07.052
72. Qi X, Xie F. Promotion effects of potassium permanganate on the removal of Pb (II), Ni (II) and Cd (II) from hydrous manganese dioxide. Chem Eng J. 2018; 351:22-30. https://doi.org/10.1016/j.cej.2018.06.042
73. Bian Y, Bian ZY, Zhang JX, Ding AZ, Liu SL, Wang H. Effect of the oxygen-containing functional group of graphene oxide on the aqueous cadmium ions removal. Appl Surf Sci. 2015; 329:269-75. https://doi.org/10.1016/j.apsusc.2014.12.090
74. Chaabane L, Beyou E, El Ghali A, Baouab MH. Comparative studies on the adsorption of metal ions from aqueous solutions using various functionalized graphene oxide sheets as supported adsorbents. J Hazard Mater. 2020; 389:121839. https://doi.org/10.1016/j.jhazmat.2019.121839
75. Park CM, Wang D, Han J, Heo J, Su C. Evaluation of the colloidal stability and adsorption performance of reduced graphene oxide-elemental silver/magnetite nanohybrids for selected toxic heavy metals in aqueous solutions. Appl Surf Sci. 2019; 471:8-17. https://doi.org/10.1016/j.apsusc.2018.11.240
76. Rout DR, Jena HM, Baigenzhenov O, Hosseini-Bandegharaei A. Graphene-based materials for effective adsorption of organic and inorganic pollutants: A critical and comprehensive review. Sci Total Environ. 2023; 863:160871. https://doi.org/10.1016/j.scitotenv.2022.160871

Supplementary References

1. Lagergren S. About the theory of so-called adsorption of soluble substances. K Sven Vetenskapsakad Handl. 1898; 24:1-39.
2. Blanchard G, Maunaye M, Martin G. Removal of heavy metals from waters by means of natural zeolites. Water Res. 1984; 18(12):1501-7. https://doi.org/10.1016/0043-1354(84)90124-6
3. Weber Jr WJ, Morris JC. Kinetics of adsorption on carbon from solution. J Sanitary Eng Div. 1963; 89(2):31-59. https://doi.org/10.1061/JSEDAI.0000430
4. Langmuir I. The constitution and fundamental properties of solids and liquids. Part I. Solids. J Am Chem Soc. 1916; 38(11):2221-95. https://doi.org/10.1021/ja02268a002
5. Freundlich H. Über die adsorption in lösungen. Z Phys Chem. 1907; 57(1):385-470. https://doi.org/10.1515/zpch-1907-5723